

3-24-2009

2-D Finite Element Modeling for Nanoindentation and Fracture Stress Analysis

Chi Chen
University of South Florida

Follow this and additional works at: <https://scholarcommons.usf.edu/etd>



Part of the [American Studies Commons](#)

Scholar Commons Citation

Chen, Chi, "2-D Finite Element Modeling for Nanoindentation and Fracture Stress Analysis" (2009).
Graduate Theses and Dissertations.
<https://scholarcommons.usf.edu/etd/1897>

This Thesis is brought to you for free and open access by the Graduate School at Scholar Commons. It has been accepted for inclusion in Graduate Theses and Dissertations by an authorized administrator of Scholar Commons. For more information, please contact scholarcommons@usf.edu.

2-D Finite Element Modeling for Nanoindentation and Fracture Stress Analysis

by

Chi Chen

A thesis submitted in partial fulfillment
of the requirements for the degree of
Master of Science in Mechanical Engineering
Department of Mechanical Engineering
College of Engineering
University of South Florida

Major Professor: Alex A. Volinsky, Ph.D.
Craig Lusk, Ph.D.
Nathan Crane, Ph.D.

Date of Approval:
March 24, 2009

Keywords: indentation test, simulation, contact mechanics, fracture, microchannel,
thermo-mechanical properties

© Copyright 2009, Chi Chen

Table of Contents

List of Tables		iv
List of Figures		v
Abstract		viii
Chapter 1	Introduction	1
1.1	Nanoindentation	1
1.2	Hertzian Contact Equations	1
1.3	Contact Between Elastic Solids	3
1.4	Elastic-plastic Contact	3
1.5	Indenters and Indenter Types	4
1.6	Load-displacement Curves	5
1.7	Factors Affecting Nanoindentation Test Data	6
1.8	The Von Mises Stress	7
1.9	Finite Element Analysis	8
1.10	Simulation of Nanoindentation Test on Thin Films Using FEM	9
1.11	Literature Review	11
1.12	Results and Discussion of Literature Results	14
1.13	Conclusions for Chapter 1	15
Chapter 2	2-D Finite Element Analysis of Nanoindentation	16
2.1	Introduction and Basic Assumptions	16
2.2	Finite Element Models	17
2.2.1	Geometry	17
2.2.2	Materials Properties	19
2.2.3	Elements and Meshing	19
2.2.4	Contact Pair and Models Summary	22
2.2.5	Boundary Conditions	23
2.2.6	Load Step and Sub Steps	23
2.3	Results and Discussion	24
2.3.1	Displacement Plot	24
2.3.2	Stress and Strain Distribution	27

	2.3.3 Load Versus Displacement Curve	30
	2.3.4 Comparison of Numerical Results and Experimental Data	33
2.4	Discussion of Numerical Results	35
	2.4.1 Effect of Tip Radius on the Simulation Results	35
	2.4.2 Effect of Gold Film Yield Strength on Simulation Results	37
	2.4.3 Other Factors Affecting the Accuracy of Simulation Results	38
	2.4.4 Identification of Elastic-plastic Transition	39
2.5	Conclusions for Chapter 2	42
Chapter 3	Finite Element Analysis of Multiple Site Damage Bonded Repair Structures	43
3.1	Introduction	43
3.2	Obtaining SIF of MSD Plate After Repair	44
	3.2.1 Displacement Method	45
	3.2.2 Stress Method	46
3.3	FE Model of the Repair Structure	46
	3.3.1 Basic Assumptions	46
	3.3.2 FE Model Validation	47
	3.3.3 Model Geometry and Materials Mechanical Properties	48
	3.3.4 Boundary Conditions for Repair Structure	49
3.4	Results and Discussion of Repair Structure Simulation	50
	3.4.1 SIF Variation With the Crack Length	50
	3.4.2 Patched and Unpatched Plates SIFs Variation With the Crack Length	52
	3.4.3 Patch Length Effect on the K Values	53
	3.4.4 Patch Thickness and Layout Effects on the K Values	55
	3.4.5 Patch Debonding	56
3.5	Conclusions for Chapter 3	57
Chapter 4	Thermo-mechanical Analysis of Porous Coatings on Steel for Catalysis Applications	58
4.1	Introduction	58
4.2	Mechanical and Other Properties of the Film/Substrate Structure	60
4.3	Problem Description	61
4.4	FEM Modeling of Micro Channel/Film Thermo-mechanical Deformation	61
	4.4.1 Basic Assumptions	61
	4.4.2 Model Validation	62
	4.4.3 Element Type and Boundary Conditions	62
4.5	Results and Discussion of Coatings in Micro Channels	63
	4.5.1 Stress Variation With the Film Thickness	63
	4.5.2 Stress Distribution Along the Path	68
	4.5.3 Process and Geometry Optimization to Avoid Failures	74

	4.5.4 Proper Materials Selection	75
	4.5.5 Strain Estimation	75
4.6	Conclusions for Chapter 4	75
Chapter 5	Summary and Future Work	76
References		78

List of Tables

Table 1.1	Pressure distribution under indentation [11].	3
Table 2.1	Materials properties [38].	19
Table 2.2	Models summary.	23
Table 3.1	Validation of the FE model.	47
Table 3.2	Materials mechanical properties [53].	48
Table 3.3	Fiber layout effect on the SIFs.	55
Table 4.1	Mechanical and thermal properties of the film and the substrate [59-63].	61

List of Figures

Fig.2.1.	Sample and indenter geometry for models 1 and 2.	17
Fig.2.2.	Sample and indenter tip geometry for models 3 and 4.	18
Fig.2.3.	Meshing density illustration in models 1 and 2.	20
Fig.2.4.	Meshing density illustration in models 3 and 4.	21
Fig.2.5.	Detailed meshing near contact area in model 2.	22
Fig.2.6.	Detailed meshing near contact area in model 4.	22
Fig.2.7.	Displacement plot for model 1 with the maximum indentation depth.	24
Fig.2.8.	Displacement plot for model 4 with the maximum indentation depth.	25
Fig.2.9.	Displacement plot for model 4 after unloading.	25
Fig.2.10.	Pile-up in model 2.	26
Fig.2.11.	The von Mises stress distribution in model 1.	27
Fig.2.12.	The von Mises stress distribution in model 2.	28
Fig.2.13.	The von Mises stress distribution in model 3.	28
Fig.2.14.	The von Mises stress distribution in model 4.	29
Fig.2.15.	Elastic strain distribution in model 4.	29
Fig.2.16.	Equivalent plastic strain distribution in model 4.	30
Fig.2.17.	Load vs. displacement curve for model 1.	31
Fig.2.18.	Load vs. displacement curve for model 3.	32

Fig.2.19.	Load vs. displacement curve for model 2.	32
Fig.2.20.	Load vs. displacement curve for model 4.	33
Fig.2.21.	Comparison of numerical results and experimental data for model 3.	34
Fig.2.22.	Comparison of numerical results and experimental data for model 4.	35
Fig.2.23.	Effect of tip radius on the simulation results of bulk quartz nanoindentation.	36
Fig.2.24.	Effect of gold film yield strength on simulation results in model 4.	37
Fig.2.25.	Comparison of numerical results and theoretical results for model 1.	39
Fig.2.26.	Comparison of FE results and theoretical results for model 2.	40
Fig.2.27.	Comparison of theoretical, numerical and experimental data for model 4.	41
Fig.2.28.	Comparison of theoretical, numerical and experimental data within the indentation depth of 20 nm for model 4.	41
Fig.3.1.	Schematics of the model geometry.	49
Fig.3.2.	a) Finite element mesh of the entire model and b) the crack tips.	50
Fig.3.3.	Comparison of the normalized SIFs values between a single crack and twin cracks of varying length.	51
Fig.3.4.	Twin cracks geometry configuration.	52
Fig.3.5.	Comparison of the SIFs values between patched and unpatched twin cracks of varying length.	53
Fig.3.6.	Effect of the patch length on the normalized SIF values of the repaired structure.	54
Fig.3.7.	Patch thickness effect on the SIFs values of the repaired structure.	56
Fig.4.1.	Planar view of the coated micro channel plate specimen.	59
Fig.4.2.	Cross-sectional optical image of 0.3×0.3 mm micro channel's profile.	59
Fig.4.3.	Cross-sectional optical image of 0.5×0.3 mm micro channel's profile.	60

Fig.4.4.	Cross-sectional optical image of 0.7×0.3 mm micro channel's profile.	60
Fig.4.5.	Finite element mesh for the 0.3×0.3 mm profile model.	63
Fig.4.6.	Effect of the film thickness on the stress at the micro channel bottom in x direction (0.3×0.3 mm).	64
Fig.4.7.	Effect of the film thickness on the stress at the micro channel side wall in y direction (0.3×0.3 mm).	65
Fig.4.8.	Effect of the film thickness on the stress at the micro channel bottom in x direction (0.5×0.3 mm).	65
Fig.4.9.	Effect of the film thickness on the stress at the micro channel side wall in y direction (0.5×0.3 mm).	66
Fig.4.10.	Effect of the film thickness on the stress in x direction at the micro channel bottom (0.7×0.3 mm).	67
Fig.4.11.	Effect of the film thickness on the stress at the micro channel side wall in y direction (0.7×0.3 mm).	67
Fig.4.12.	The 1 st and 2 nd principal stress distribution along the path.	69
Fig.4.13.	The 1 st principal stress distribution along the path with different film thickness (0.3×0.3 mm).	70
Fig.4.14.	The 1 st principal stress distribution along the path with different film thickness (0.5×0.3 mm).	71
Fig.4.15.	SEM image of cracked 0.5×0.3 mm micro channel lower end.	72
Fig.4.16.	The 1 st principal stress distribution along the path with different film thickness (0.7×0.3 mm).	73
Fig.4.17.	Comparison between FE results and the SEM image of cracked 0.7×0.3 mm micro channel lower end.	73
Fig.4.18.	Stress distribution along the path with the same film thickness in different models.	74

2-D Finite Element Modeling for Nanoindentation and Fracture Stress Analysis

Chi Chen

ABSTRACT

In Chapter 1, a brief introduction of nanoindentation and finite element method is presented. General procedures have been developed based on FEM modeling of nanoindentation data to obtain the mechanical properties of thin films. Selected FEM models are illustrated in detail.

In Chapter 2, nanoindentation test is simulated using finite element method based on contact mechanics approach. The relationship between load and indentation depth is obtained. The numerical results show good agreement with experimental data. It is shown that FEM is an effective tool for simulation of nanoindentation tests of metallic films. However, limitations caused by simplification of models and assumptions should not be neglected.

In Chapter 3, finite element method is used to analyze bonded repair structure of aluminum plates with Multiple Site Damage (MSD). A 2-D 3-layer technique is used to deal with the damage area. A typical aluminum plate with multiple collinear twin cracks is taken as an example. The effects of relative position of two cracks, patch size, and patch thickness on stress intensity factors are studied in detail. The results reveal that the

stress intensity factors at the tips of collinear twin cracks can be reduced greatly through bonded composite repair. In order to increase the performance of the patch repair, the adhesive properties, the patch length and thickness must be optimized.

In Chapter 4, finite element method is used for thermo-mechanical analysis of porous coatings in steel micro channels used for catalysis. Thermal stresses in the coating due to temperature changes are obtained. The effects of micro channel geometry on thermal stresses are studied in detail. The results reveal that in order to increase the mechanical performance of the coatings, film thickness and profile geometry must be optimized.

Chapter 5 summarizes major results and outlines future work.

Chapter 1 Introduction

1.1 Nanoindentation

Indentation is a simple and commonly applied method to test the mechanical properties of materials. In indentation testing, the material of interest with unknown mechanical properties (e.g. elastic modulus and hardness) is contacted by another material with known mechanical properties. The technique originates from Mohs scale of mineral hardness introduced in 1812 [1, 2]. For conventional indentation test, the length scale of the penetration is measured in microns or millimeters. More recently, nanoindentation, an indentation test in which the length scale of the penetration is measured in nanometers, has been established as a basic tool for investigating the mechanical properties of small volumes of material [3-5]. Nanoindentation technique can be used to calculate not only hardness but also elastic modulus, strain-hardening exponent, fracture toughness (for brittle materials), and viscoelastic properties [6].

1.2 Hertzian Contact Equations

The analysis of indentation test is based on the theory of contact mechanics [7]. Hertz [8, 9] studied the contact between a rigid sphere and a flat surface and found that the radius of the contact circle a is related to the indenter load F , the indenter radius R , and the elastic properties of the materials as:

$$a^3 = \frac{4 kFR}{3 E} \quad (1.1),$$

where k is an elastic mismatch factor given as:

$$k = \frac{9}{16} [(1 - \nu^2) + \frac{E}{E'} (1 - \nu'^2)] \quad (1.2).$$

In Eq.1.2, E, ν and E', ν' are the Young's modulus and Poisson's ratio for the specimen and the indenter, respectively. Hertz also found that the maximum tensile stress in the specimen occurs at the edge of the contact circle at the surface and is given by:

$$\sigma_{max} = (1 - 2\nu) \frac{F}{2\pi a^2} \quad (1.3).$$

The maximum tensile stress outside the indenter can be expressed in terms of the indenter radius R:

$$\sigma_{max} = \left[\frac{(1-2\nu)P}{2\pi} \right] \left(\frac{3E}{4k} \right)^{\frac{2}{3}} F^{\frac{1}{3}} R^{-\frac{2}{3}} \quad (1.4).$$

The mean contact pressure, P_m , is given by the indenter load divided by the contact area.

$$P_m = \frac{F}{\pi a^2} \quad (1.5).$$

It can be shown from Eq.1.1 that the contact area is proportional to $F^{\frac{2}{3}}$ and therefore P_m is proportional to $F^{\frac{1}{3}}$. Substituting Eq.1.5 into Eq.1.1 gives:

$$P_m = \left(\frac{3E}{4\pi k} \right) \frac{a}{R} \quad (1.6).$$

It is more useful to relate the load F to the indentation depth h as below:

$$F = \frac{4}{3} E_r R^{\frac{1}{2}} h^{\frac{3}{2}} \quad (1.7),$$

where E_r is the reduced modulus of the material being indented [10].

1.3 Contact Between Elastic Solids

There are several assumptions in the analysis of the indentation process and the contact between elastic solids:

-Compared with the radius of the contact circle, the dimensions of each body are large. With this assumption, each surface can be considered as an elastic half space.

-The contact between the two bodies is frictionless.

-There is only a normal pressure transmitted between the indenter and the specimen.

Table 1.1 summarizes the distribution of surface normal pressures to be considered.

Table 1.1 Pressure distribution under indentation [11].

Indenter type	Equation for normal pressure distribution $r < a$
sphere	$\frac{\sigma_z}{P_m} = -\frac{3}{2} \left(1 - \frac{r^2}{a^2}\right)^{\frac{1}{2}}$
cone	$\frac{\sigma_z}{P_m} = -\cosh^{-1} \frac{a}{r}$

1.4 Elastic-plastic Contact

The elastic stress fields generated by an indenter are relatively simple compared to the elastic-plastic stress fields. Theoretical treatments mentioned above are limited in the case of elastic-plastic problems due to their complexity. Numerical methods, like finite element method, are widely used to analyze elastic-plastic indentations [11].

1.5 Indenters and Indenter Types

Indenters are usually made of diamond. Diamond indenters are very hard, but are also very brittle and can be broken easily. The mechanical properties of diamond vary due to the crystalline nature of the diamond structure. Values for modulus range from about 800 GPa to 1200 GPa in literature. A value of 1000 GPa is usually used in the analysis of nanoindentation test data with a Poisson's ratio of 0.07 [1].

The main aim of the nanoindentation tests is to obtain the elastic modulus and hardness of the specimen material through load-displacement measurements. The depth of penetration beneath the specimen surface is measured as the load is applied to the indenter. Therefore, the size of contact area can be determined by the known geometry of the indenter. There are several types of indenters used in nanoindentation testing. Indenters can be classified into two categories: sharp or blunt. Generally speaking, pyramidal and conical indenters are sharp, and spherical indenters can be considered as blunt.

The Berkovich indenter is generally used in small scale indentation testing [12]. It has the advantage that edges of the three-sided pyramid are more easily constructed to meet at a single point compared to those edges of the four-sided Vickers pyramid. The face angle of the Berkovich indenter normally used in nanoindentation testing is 65.27 degrees. The tip radius for a new Berkovich indenter is about 50-100 nm, which usually increases to about 200 nm with use [1].

Conical indenters have the advantage of axial symmetry. For a Berkovich indenter, the equivalent conical indenter has a semi-angle of 70.3 degrees [1, 13]. When analyzing nanoindentation test data taken with Berkovich indenters, it is convenient to use an

equivalent axial-symmetric conical indenter for simplification [13]. Spherical indenters are especially suitable for testing soft materials. This type of indenters provides a smooth transition from elastic to elastic-plastic contact [14].

1.6 Load-displacement Curves

In a typical nanoindentation test, the load and the depth of penetration are recorded. In the loading process, the load is applied from zero to a maximum value in small increments. Then in the unloading process, the load decreases from the maximum value back to zero. If the plastic deformation occurs, then a residual deformation is left in the surface of the specimen. Since the size of the residual deformation for nanoindentation testing is very small, it cannot be measured accurately by optical techniques. Thus, the known geometry of the indenter and the penetration depth provide the indirect method to estimate the contact area when indenting a material with known elastic modulus [15].

In the unloading process, when the load is removed from the indenter, the specimen material attempts to recover to its original shape. However, this recovery cannot be made fully because of plastic deformation. Only some extent of recovery will be realized due to the relaxation of elastic strains. This explains why in the load-displacement curve of plastic nanoindentation testing, the loading and unloading parts of the load-displacement curve do not coincide.

1.7 Factors Affecting Nanoindentation Test Data

There are various errors associated with the nanoindentation testing procedure [14, 16-20]. For example, the offsets to the depth measurements, the environmental changes during the test, the non-ideal shape of the indenter, and some materials related issues will affect the results validity. Some of the factors which are most commonly encountered in experimental and numerical analysis are listed below.

-Initial penetration depth: Ideally, the indenter displacement in a nanoindentation test is measured from the top surface of the specimen. In practice, however, before the displacement measurements can be done, the indenter must contact the specimen surface first. So an initial contact depth appears and is usually set to be as small as possible. In the experiments, the initial contact force which will result in the initial penetration is set to about $1 \mu\text{N}$. To avoid this error, a small initial depth has to be added to all displacement measurements [1].

-Indenter geometry: In practice, the geometry of the indenter may not be ideal. Many factors, including crystal anisotropy of diamond indenters, may affect the standard shape of the indenter. So a correction factor is needed to deal with the problems caused by non-ideal geometry of the indenter used in practical tests [1]. The correction factor can be found from AFM or SEM measurements of the indenter geometry. Further, the area function of the indenter can be obtained [21].

-Pile-up and sink-in: The specimen material may either sink in, or pile-up around the indenter when plastic deformation appears [3, 18]. The degree of pile-up or sink-in depends on two factors. One is the ratio E/Y (E is Young's modulus and Y is yield strength) of the specimen material and the other is the strain-hardening exponent x . For

non-strain-hardening materials with a large value of E/Y , pile-up is to be expected [3]. The plastic zone of this kind of materials is observed to have a hemispherical shape with a range far beyond the contact radius, while most of the plastic deformation occurs near the indenter. For materials with a low value of E/Y , sink-in is more likely to occur. The plastic zone of this kind of materials is typically contained within the boundary of the contact radius. In nanoindentation, the elastic deformations are spread at a greater distance from the indenter.

-Tip rounding: The three-sided Berkovich diamond pyramid may be the most commonly used indenter in nanoindentation testing. In practice, such indenters are not perfectly sharp. Usually they have a tip radius around 100 nm [16, 22]. Tip rounding becomes important in two situations. One is when the thin films under indentations are no thicker than 500 nm. The other is when the maximum depth of penetration is about 50 nm. An initial elastic contact may be caused by the tip rounding. The hardness measurement data obtained may thus be in error because the mean contact pressure may be larger than the expected value [1].

1.8 The Von Mises Stress

In engineering the von Mises yield criterion [23-25] can be also formulated as the von Mises stress or equivalent tensile stress. It is a scalar stress value which can be computed from the stress tensor. A material will start yielding when its von Mises stress reaches a critical value (yield strength). The von Mises stress is applicable for the plastic deformation analysis for ductile materials such as metals.

1.9 Finite Element Analysis

As a computer simulation technique, finite element analysis (FEA) is widely used in engineering [26]. There are many finite element commercial software packages, such as ANSYS, ABAQUS, and NASTRAN. An energy principle, like virtual work principle or the minimum total potential energy principle, is usually the base for the development of those finite element software packages [24].

In its applications, the object or system is described by a simplified geometrical model. The model is discretized to many small and linked regions-i.e., finite elements on an unstructured grid. For every single element, there are corresponding equations of equilibrium, in conjunction with applicable physical considerations such as compatibility and constitutive relations. In this way a group of simultaneous equations is established. The unknown values of the group of equations are solved using the techniques of linear algebra or non-linear numerical methods. As an approximate method, the accuracy of the FEA can be improved by refining the mesh in the model using smaller elements and more nodes.

FEA is commonly used in mechanical systems for the determination of stresses and displacements. However, it can also be used in the analysis of many other problems in different areas, including heat transfer, contact mechanics, fluid dynamics, and electromagnetism. The advantage of FEA is that it can handle complex problems which are difficult to solve analytically [26].

1.10 Simulation of Nanoindentation Test on Thin Films Using FEM

With the rapid development of finite element analysis programs, it is reasonable to simulate the load-displacement responses for materials during nanoindentation processes [27-29].

The elastic stress fields around the contact area between an indenter and specimen materials are complex but well defined, no matter what type the indenter is used. However, if the response of the specimen material is not elastic, say elastic-plastic or viscoelastic, it is usually difficult to obtain simple theoretical results of stress fields around the contact area [11]. Nanoindentation testing with a sharp pyramidal indenter, such as Berkovich or Vickers, is one of the most complex contact mechanics problems. This is due to the 3 dimensional phenomenon associated with large elastic or elastic-plastic deformations [30]. In this case, finite element analysis can provide valuable results to show the displacement and stress distribution of the specimen material during both loading and unloading processes. For more than ten years, finite element analysis has been widely used in the area of nanoindentation simulation [14, 31, 32].

In the analysis, load applied to the indenter can be force or displacement load. Both of them should be applied in a series of increments. Every step of displacement should be very small. If this is not the case, the program will not run smoothly. For nanoindentation simulation, large deformation, and geometric considerations must be included in the analysis [29, 33].

To reduce the calculation time, the mesh density of the numerical model should not be uniform. The density of nodes and elements at and near the contact area of interest must be higher than other areas of the model. In this way the localized deformation of

the specimen material can be presented accurately and clearly [19, 34]. In the analysis, the dimensions of specimen like substrate thickness should be large enough in order to represent an infinite half space. If the outer boundaries of the model are not far away from the contact, accuracy of the results will be affected.

As for the post process of finite element analysis, displays of displacement and stress distribution are sufficient for many cases. Stress concentrations can be identified easily from those plots. For nanoindentation application, the load-displacement curve is the most important. There are several ways to get the curve, depending on the type of the loading used in the model.

Generally there are three steps to setup the simulation. The first step is to establish a geometric model that can describe the indenter and specimen as closely as possible [32]. All the geometric parameters including the film thickness and indenter area function should be obtained. Appropriate indenter tip radius should be estimated.

The next step is to determine the mechanical properties for all the materials. Usually the materials in the model are isotropic, elastic or elastic-plastic solids. Young's modulus, Poisson's ratio, and a stress-strain curve for the elastic-plastic material should be obtained.

The final step is to determine the interactions between all surfaces. The interface between the thin film and the substrate are usually defined as perfectly bonded. There is no delamination or slippage at the interface. The interaction between the indenter tip and the top surface of the specimen is defined as a sliding surface with or without friction.

1.11 Literature Review

In previous works [13, 35, 36], finite element simulation technique was employed to investigate the effects of the mechanical properties of the substrate, the critical ratio of coating thickness to indentation depth, the friction coefficient between the indenter and the surface. Sun et al. [35] investigated the nanoindentation process, which involved a hard coating on a soft substrate. The indenter was assumed to be rigid and the contact between the indenter and specimen materials was frictionless. An ideally axisymmetric conical indenter with the same area-depth function as a Berkovich indenter was used in order to simplify the analysis to a 2-D axisymmetric problem. The authors claimed that this would not cause any noticeable difference in the load-displacement response of the materials. Berkovich indenter geometry would result in an elastic singularity at its edges in numerical simulation but this equivalent conical model would only affect the stress-strain response of a few of the elements adjacent to the indenter edges.

The semi-infinite layered medium was modeled by hundreds of 8-node, isoparametric quadrilateral axisymmetric elements. To determine the stress field in the highly stressed zone, very fine mesh was used in the coating and the substrate near the coating/substrate interface around the contact zone. Relatively coarse mesh was used beyond the contact zone and the coating/substrate interface to reduce computation time. Dozens of 4-node, axisymmetric interface elements were used to detect the contact between the rigid indenter and the coating surface. The rigid indenter with various tip radii was simulated. There were round tips of radius 0.2, 0.5, 1.0 and 2.0 μm , and a perfectly sharp tip. The area-depth function of a round tip has been discussed by Shih et al. [16]. The program was made to detect and monitor the contact or separation between

the surface nodes and the rigid surface automatically. Two sets of elements were used to define the elastic and plastic properties of the coating and the substrate materials separately.

The large strain elastoplastic feature of the ABAQUS finite element package was used to simulate the indentation process defined in the model. An updated Lagrangian formulation was adopted in the program due to the large displacements which may arise beneath the indenter during plastic deformation.

K.C. Tang [36] made a comparison between a purely elastic analytical model and an elastic-perfectly plastic finite element model for a spherical indenter on a multi-layered substrate. The commercial ANSYS finite element code was employed to investigate the indentation problem of a spherical indenter contacting an elastic film/elastic-perfectly plastic substrate structure. Only one-half of the semi-infinite solid was modeled due to symmetry. 2-D, 8-node structural solid elements were used in the finite element model. A 2×2 integration scheme was used for the 8-node elements. Between the top surface of the layer and the elastic indenter there were thousands of 2-D point-to-surface contact elements. Thus, contact can be detected by following the positions of points on one surface relative to lines (or areas) of another surface with the help of those contact elements. Appropriate forces can be applied to nodes on the two surfaces whenever contact was detected.

A refinement of the mesh near the contact area was necessary in order to accurately predict the pressure distribution, contact area and the stress-strain fields in the highly stressed region around the contact zone. Hence, the smallest elements were set immediately beneath the contact surface. The x and y dimensions of those elements were

1 μm each. The finite element mesh has the ability to vary this finely meshed area while keeping the size of the half space constant depending on the extent of the contact zone. A graduated mesh was constructed in order to reduce the computational time. 2-D quadrant elements were employed to mesh the elastic indenter. The round tip radius was assumed as 100 μm to represent a scratch test indenter.

The first five rows of elements along the top of the half space were assigned to be the single layer. The elements were assumed to be perfectly bonded to the substrate at the interface. The advantage of this finite element model was that the thickness and the number of elements across the layer can be changed according to the requirement of different applications. Additional layers can also be added to the model.

Lichinchi et al. [13] studied the Berkovich nanoindentation process using the finite element analysis. They verified that a 2-D axisymmetric model can give the same results of the load–displacement curve as a 3-D model in the condition that the equivalent conical indenter has the same area function as a Berkovich tip. Since the 2-D axisymmetric model has less degrees of freedom and requires shorter computational time, it was used for all the analyses presented in this paper. The load-displacement curves simulated with the three dimensional model were actually the same as the corresponding data obtained with a 2-D axisymmetric model. The authors concluded that to reproduce the mechanical response of a sharp Berkovich indenter, an equivalent conical indenter with a semi-apical angle $\theta = 70.3^\circ$ can be used in finite element approach.

1.12 Results and Discussion of Literature Results

The results of Sun et al. [35] showed that the finite element analysis is a useful technique when applied to the nanoindentation process on various hard coating/soft substrate systems. The analysis revealed that the critical ratio of coating thickness to indentation depth is a function of the yield strength ratio of the coating to the substrate and the indenter tip radius.

The analytical and finite element results within the elastic range obtained by K.C. Tang et al. [36] showed good agreement along the axis of contact and at the coating surface. However, the analytical results differed from numerical results beyond the elastic limit, since the analytical model failed to represent plastic behavior. The finite element results also showed that the elastic deformation of the indenter cannot be neglected for large indentation depth where plasticity effects are dominant.

Comparison between the results for the rigid tip and deformable tip models obtained by Lichinchi et al. [13] showed no relevant differences. The only significant discrepancy is that the maximum load value was slightly higher in the case of the deformable tip. This is due to the partial absorption of the deformation energy from the indenter.

However, the finite element models introduced may not be perfect. There are many limitations of this kind of method in nanoindentation simulations. Some are caused by the simplified assumptions and limitations of the approximate finite element calculation. Some are due to unknown properties of the specimen materials. The rigid body assumption for the diamond indenter may not be appropriate when the specimen is very hard. In this situation, the elastic strain of the indenter cannot be neglected [37].

Bonding between layers in the specimen is assumed to be perfect, i.e., no delamination can occur. However, in practice, debonding can occur during nanoindentation testing. Some of the uncertainties which may be present for the specimen materials include:

- The unknown preexisting residual stress of the specimen materials;
- Anisotropic properties of the materials (this could be treated in a 3-D calculation);
- The geometry dimensions data used in the model, such as layer thickness, may not be accurate;
- The top surface of the specimen materials may be a rough surface.

1.13 Conclusions for Chapter 1

The finite element method has been widely used to simulate the elastic and plastic deformations beneath a pointed indenter in nanoindentation test. Finite element simulation can offer many advantages. With this method, the time spent for the experiment can be reduced. Large scale finite element commercial codes can provide simulation environment for various physical models of indenter tips, films and substrates. In some previous work, the numerical results showed satisfactory agreement with the experimental data. However, simplified models, idealized assumptions and uncertainty of material properties may result in error for the numerical analysis. Further research is necessary to simulate nanoindentation with fewer limitations.

Chapter 2 2-D Finite Element Analysis of Nanoindentation

2.1 Introduction and Basic Assumptions

Indentation simulation based on contact analysis is a highly nonlinear problem. Due to this complexity, the commercial FE package ANSYS 11.0 was used to model the large deformation problem of nanoindentation. In this work, 4 different 2-D axisymmetric FE models are presented. Model 1 and model 2 are used to simulate nanoindentation of bulk materials and thin film/substrate materials with spherical indenters. Model 3 and model 4 are used to simulate conical nanoindentation on bulk materials and thin film/substrate materials, respectively.

There are several basic assumptions for the simulations. First, the interface of thin films and substrates is assumed to be perfectly bonded. There is no delamination or slippage at the interface. Second, the contact between the indenter and the top surfaces of the bulk material or thin film is assumed to be frictionless, since the effect of friction between the indenter tip and the surfaces of the bulk material or thin film in nanoindentation process is negligible due to small scale [22].

2.2 Finite Element Models

2.2.1 Geometry

Geometry of model 1 and 2 is shown in Fig.2.1. The spherical indenter has a diameter of 200 nm. The bulk material in this model is set to be a cylinder of 2000 nm diameter with the thickness of 1000 nm. These dimensions are large enough to simulate a semi-infinite half space for indentation with a maximum depth of 90 nm in this model.

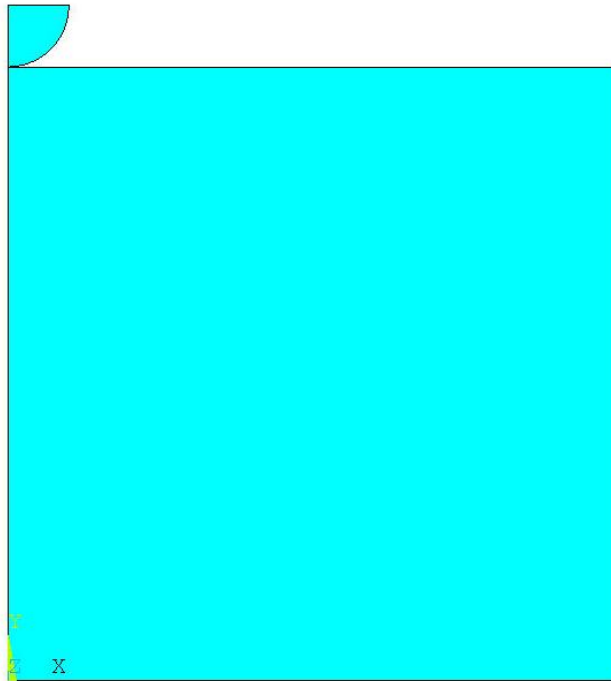


Fig.2.1. Sample and indenter geometry for models 1 and 2.

The spherical indenter in model 2 has a diameter of 400 nm. The thin film/substrate materials are modeled as cylinders with 4000 nm diameter. The thin film

has a thickness of 200 nm. The total thickness (thin film + substrate) is 2200 nm. In this model, the maximum indentation depth is 100 nm.

Geometry of model 3 is shown in Fig.2.2. The conical indenter has a semi-vertical angle of 70.3 degrees. In this way, it can be used to approximate the three-sided pyramid Berkovich indenter since it gives the same depth-area function as the Berkovich indenter. The indenter tip radius is 5 nm. The diameter of bulk material cylinder is 1000 nm. The thickness of the bulk material is 1000 nm. The maximum indentation depth is 90 nm.

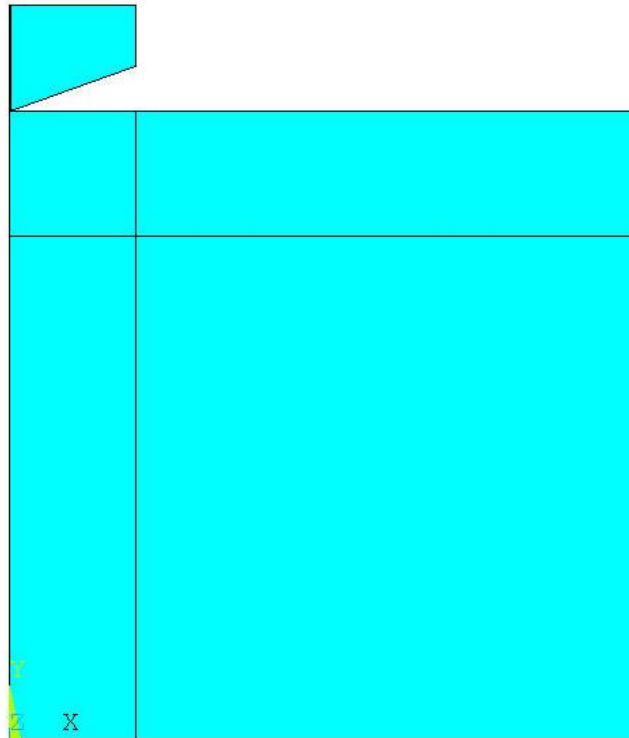


Fig.2.2. Sample and indenter tip geometry for models 3 and 4.

Same as in model 3, the semi-vertical angle of the conical indenter in model 4 is 70.3 degrees. The indenter tip radius is 100 nm. The thin film/substrate materials are

modeled as cylinders with 4000 nm diameter. The thin film has a thickness of 200 nm. The total thickness (thin film + substrate) is 2200 nm. In this model, the maximum indentation depth is 85.3 nm.

2.2.2 Materials Properties

In this work, the finite element analysis of nanoindentation problems is based on continuum mechanics. The diamond indenters in all the models and the bulk quartz in model 1 and 3 are defined as isotropic elastic materials. The gold film in models 2 and 4 is defined as isotropic elastic-perfectly plastic material. The mica substrate in models 2 and 4 is defined as isotropic elastic materials. The materials properties in all the models are listed in Table 2.1.

Table 2.1 Materials properties [38].

Material	Young's modulus E (GPa)	Initial yield stress Y (MPa)	Poisson's Ratio ν
Diamond indenter	1140		0.07
Bulk quartz	72		0.17
Gold film	78	205	0.44
Mica substrate	169		0.25

2.2.3 Elements and Meshing

In this work, three kinds of elements are employed to build the models. 2-D 4-node planar element PLANE182 is used to model all the areas of indenter, bulk material,

and film/substrate materials. This element type is chosen due to its axisymmetric modeling function. It is capable of being used in cases of large deflection and large strain. Besides, it can be coupled with CONTA171 and TARGE169 elements to define a contact pair [39]. The contact element TARGE169 is employed at the indenter surface. The contact element CONTA171 is used at the upper surface of bulk materials or thin films.

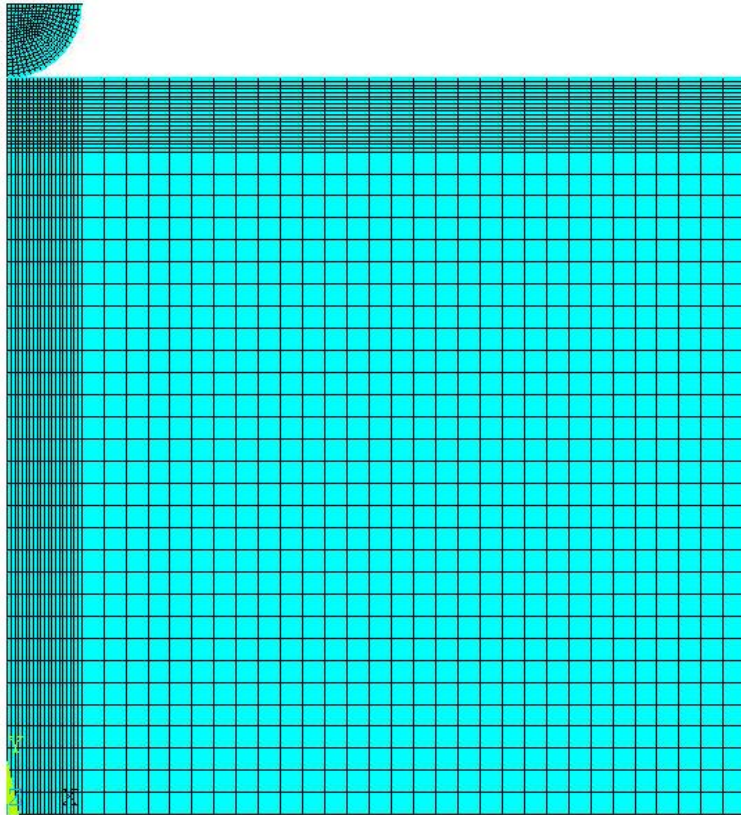


Fig.2.3. Meshing density illustration in models 1 and 2.

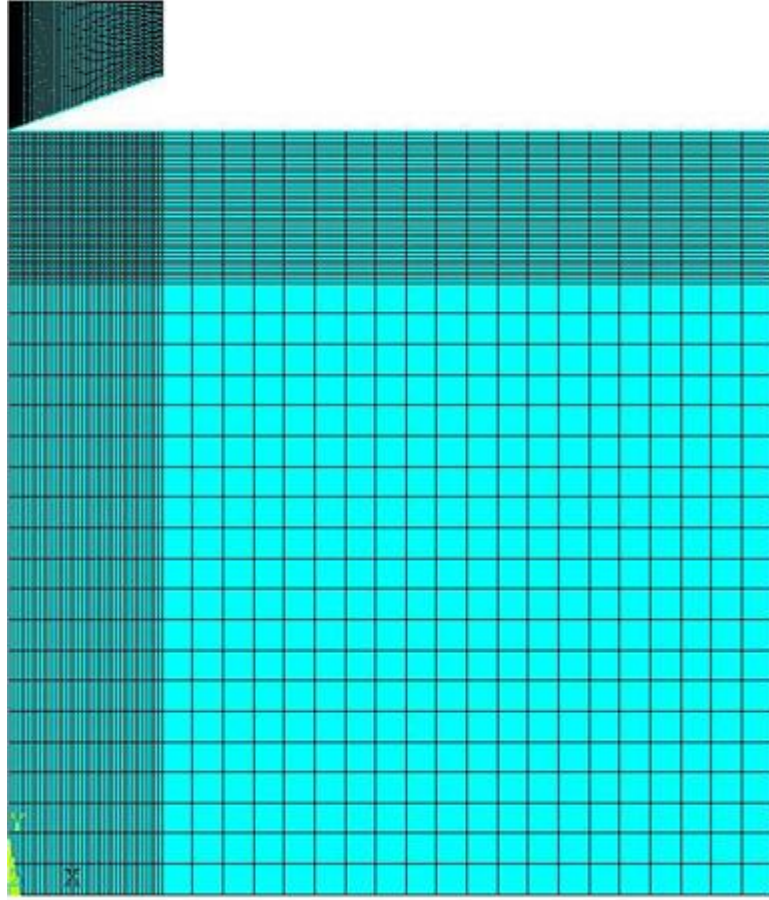


Fig.2.4. Meshing density illustration in models 3 and 4.

Fig.2.3 to Fig.2.6 illustrate the finite element meshing in every model. There are 3 different meshing density zones present. The contact area has the finest mesh. The smallest element size of the contact surface is $2.5 \text{ nm} \times 2.5 \text{ nm}$. Fig.2.9 and Fig.2.10 show the detailed mesh around the contact area between the indenter and the thin film/substrate materials.

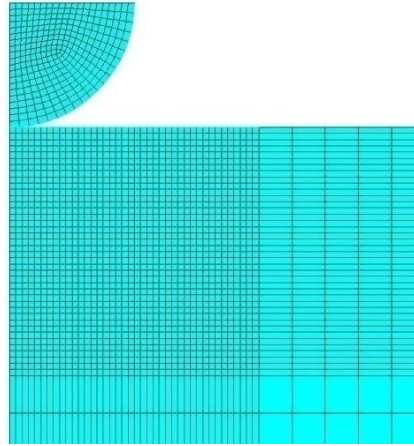


Fig.2.5. Detailed meshing near contact area in model 2.

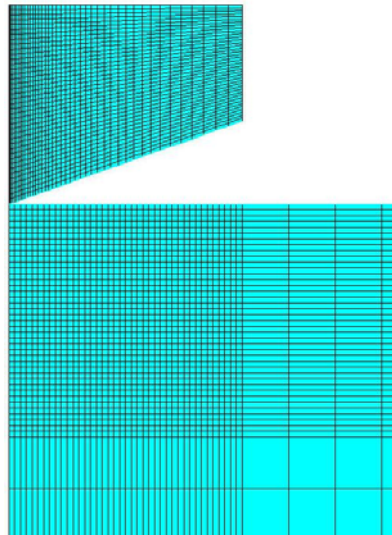


Fig.2.6. Detailed meshing near contact area in model 4.

2.2.4 Contact Pair and Models Summary

The bottom surface of the indenter and the top surface of bulk materials formed a contact pair in model 1 and 2. The bottom indenter surface and the thin film top surface formed a contact pair in model 3 and 4. Models summary is listed in Table 2.2.

Table 2.2 Models summary.

Model	Indenter type	Specimen materials
1	Spherical	Bulk quartz
2	Spherical	Gold film/mica substrate
3	Conical	Bulk quartz
4	Conical	Gold film/mica substrate

2.2.5 Boundary Conditions

Along the axis of symmetry, roller boundary conditions are applied. All the nodes on the y axis can only have the displacement in y direction. The x direction displacement is set to zero. The bulk material or substrate base is constrained by fixed boundary conditions. All the nodes on the base cannot move in any directions.

All the nodes on the upper surface of the indenter are coupled together. In this way, those nodes have the same y displacement. The load applied to the indenter is the displacement load. This kind of load can help avoid the convergence problems caused by initial contact gap.

2.2.6 Load Step and Sub Steps

There are two load steps used in the models: loading and unloading. The loading behavior of nanoindentation is simulated by increasing the indenter displacement in small increments. During the loading step, the indenter is applied a y direction displacement and contact the bulk material or thin film up to the maximum indentation depth. During the unloading step, the indenter returns to its original position incrementally. The y

direction displacement applied to the indenter in this load step is set to be zero. To solve these nonlinear large strain problems, maximum number of sub steps cannot be too small. In model 4, for loading step, maximum sub step number is set to 200. The actual number of sub step used in the program is 95.

2.3 Results and Discussion

2.3.1 Displacement Plot

In Fig.2.7 one can see the deformation of bulk quartz in model 1 when the indentation depth reaches its maximum. Due to the elastic properties of bulk quartz, the deformation reduced to zero after unloading. The shape of bulk material recovered completely to its original condition. In model 3, the result is similar.

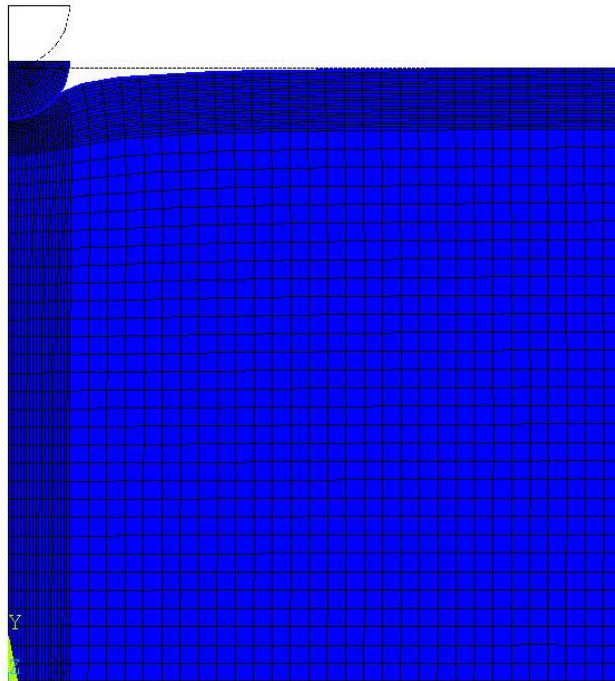


Fig.2.7. Displacement plot for model 1 with the maximum indentation depth.

In models 2 and 4, things are different. Fig.2.8 shows the deformation of thin film/substrate materials when the indenter had the largest displacement in model 4. Then, after unloading step, the substrate recovered. But the deformation of the thin gold film cannot recover due to plasticity. Fig.2.9 shows this situation after unloading in model 4.

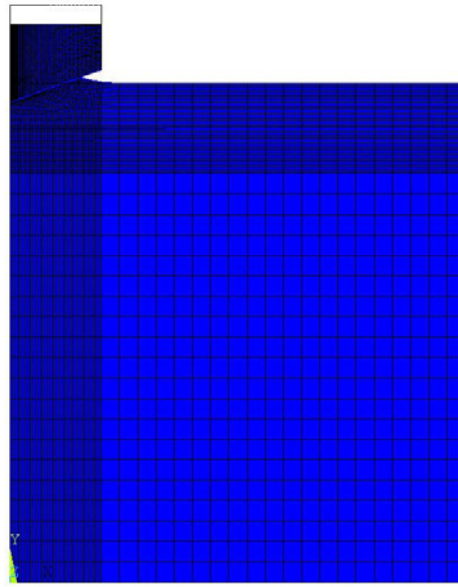


Fig.2.8. Displacement plot for model 4 with the maximum indentation depth.

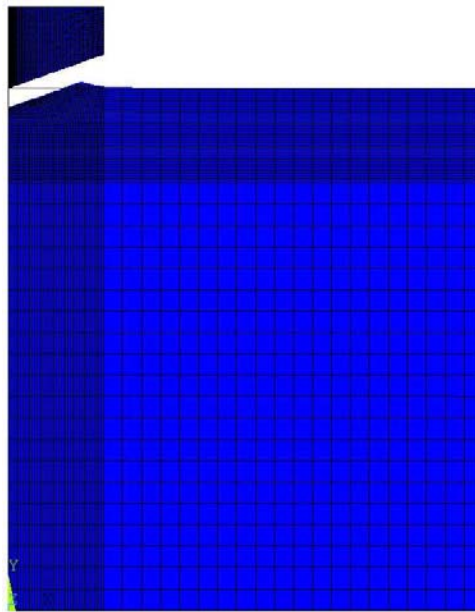


Fig.2.9. Displacement plot for model 4 after unloading.

From Fig.2.8 to Fig.2.10 one can see significant “pile-up” around the indenter tip. For soft film/hard substrate materials (gold/mica) in models 2 and 4, the deformation downward into the soft film is constrained by the hard mica substrate. The gold film under contact pressure tends to move upward. In this way, the pile-up phenomenon occurs. Many metallic materials (particularly with low work-hardening coefficients) do indeed pile-up around indenter tips during a nanoindentation test [1, 3].

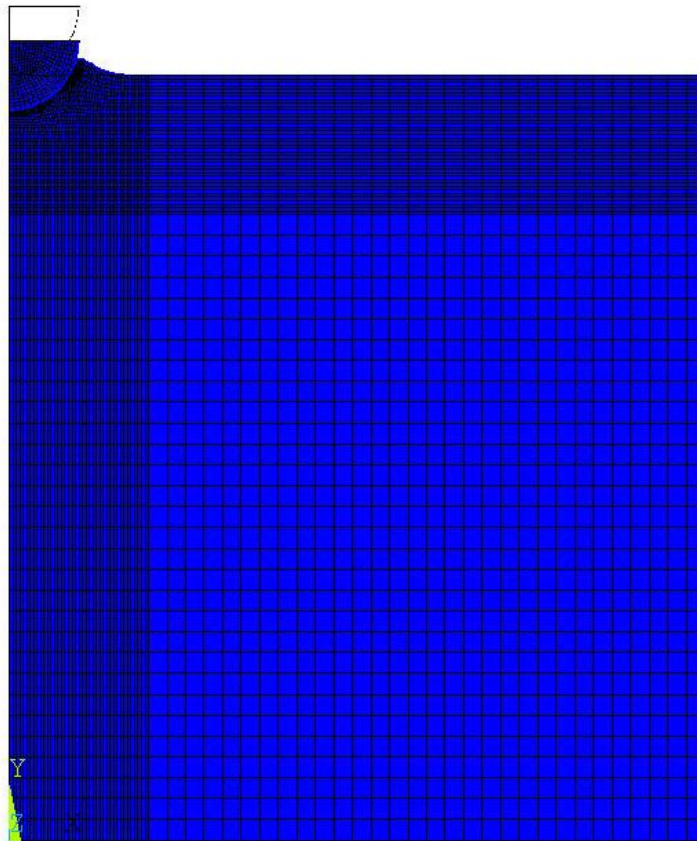


Fig.2.10. Pile-up in model 2.

2.3.2 Stress and Strain Distribution

The von Mises equivalent stress distributions in models 1 to 4 are presented in Fig.2.11 through Fig.2.14. The indenter is positioned at 90, 100, 90, 85.3 nm (maximum displacement), respectively.

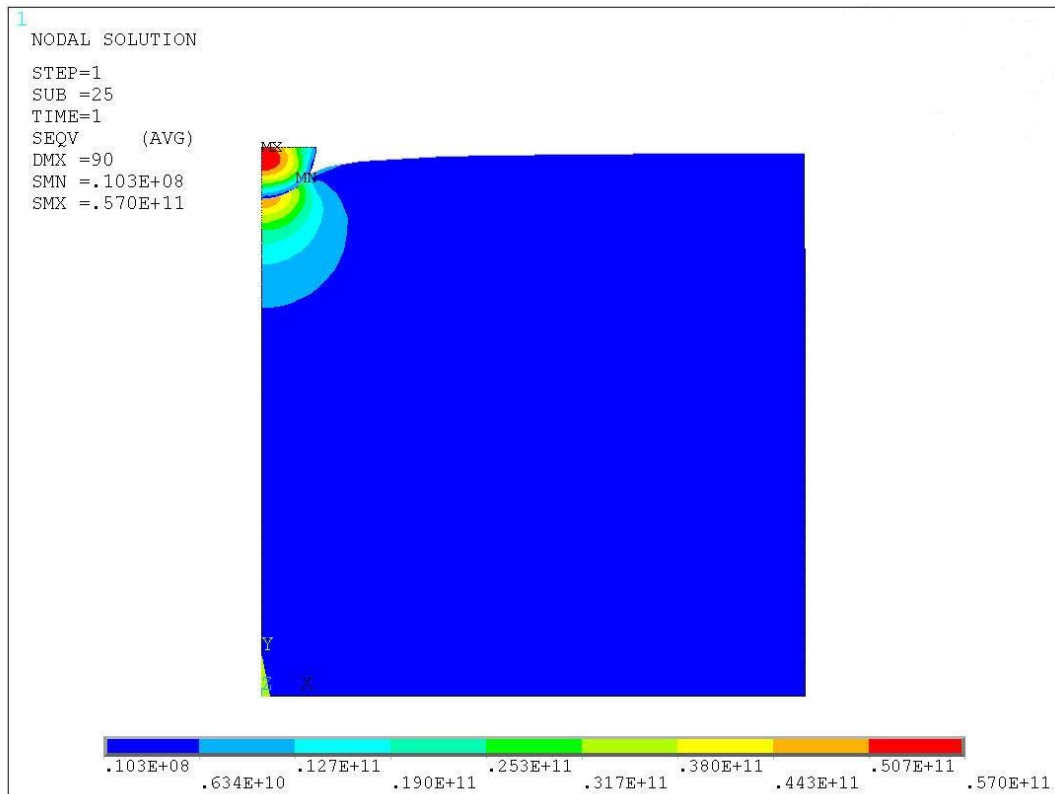


Fig.2.11. The von Mises stress distribution in model 1.

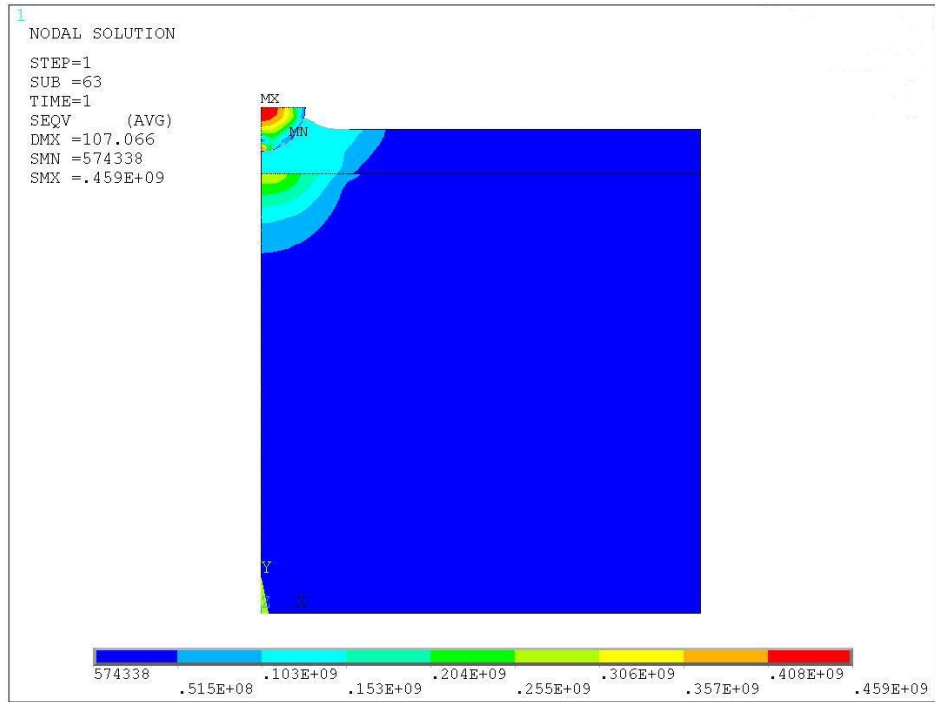


Fig.2.12. The von Mises stress distribution in model 2.

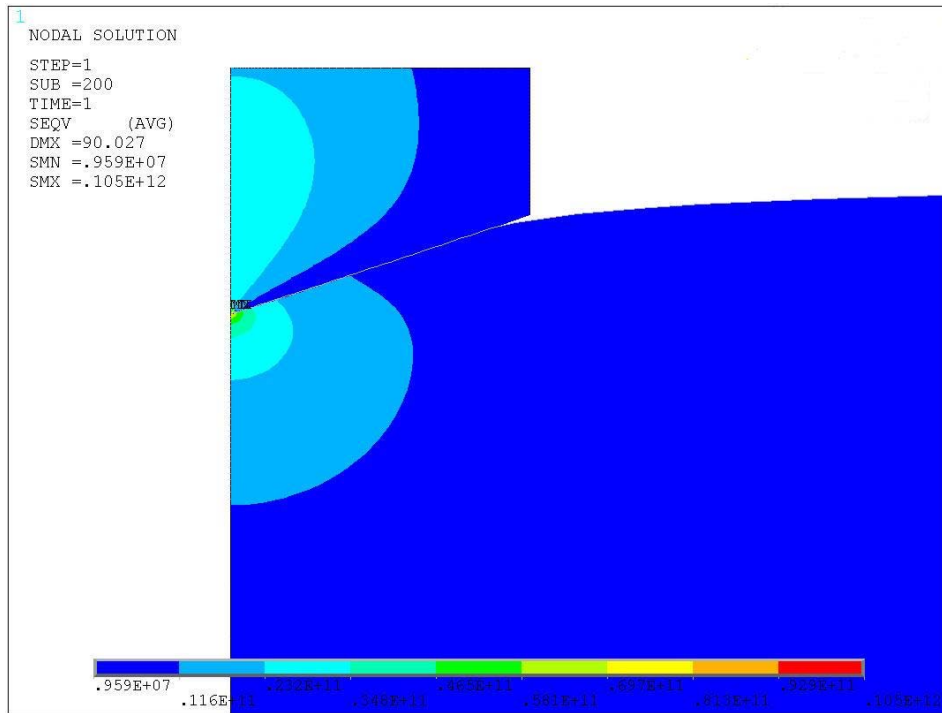


Fig.2.13. The von Mises stress distribution in model 3.

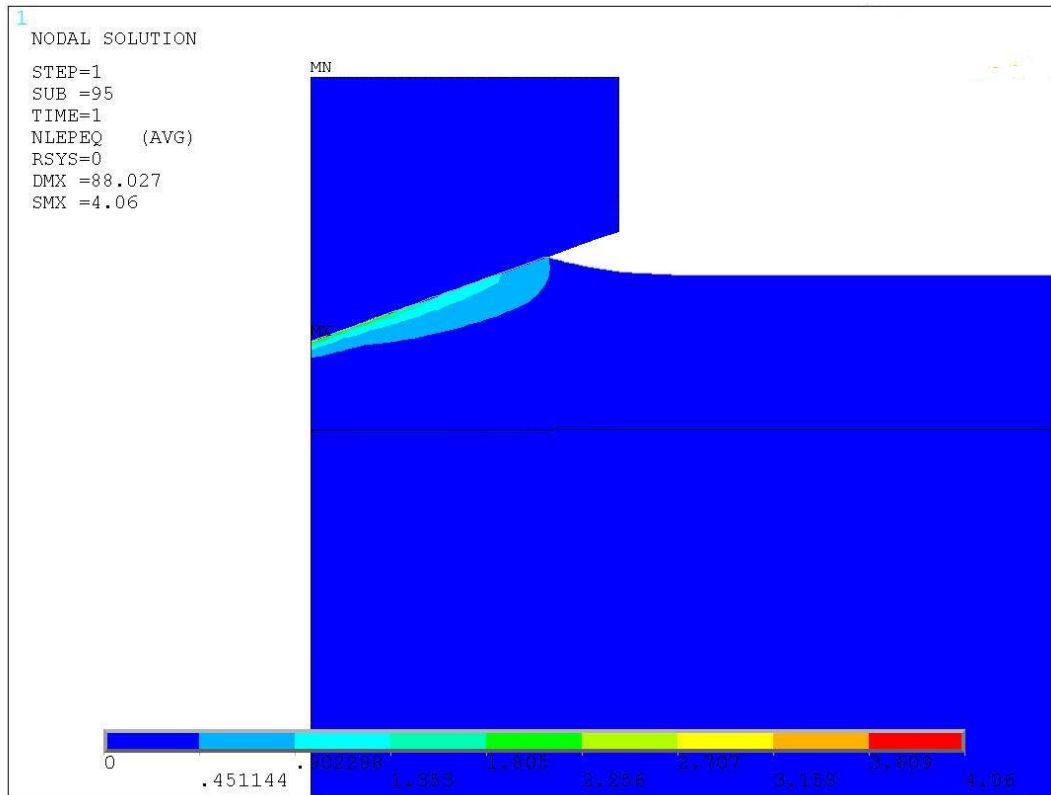


Fig.2.16. Equivalent plastic strain distribution in model 4.

Although the stress in the indenter tip is high, the strain remains nearly zero. This is why in many simulations, diamond indenter with the Young's modulus of 1140 GPa is often considered as rigid body. Using a pilot node and rigid surface, there's no need to mesh the indenter with the PLANE182 element. The number of elements can be reduced and the simulation can be simplified in this way [28]. However, in the case of superhard coatings indentation, rigid surface cannot be used to simulate the indenter [37].

2.3.3 Load Versus Displacement Curve

In this work, the indenter is imposed with a downward displacement to simulate the loading step of nanoindentation. Getting the corresponding load value for a given

indenter displacement is complicated due to the contact area calculation. To avoid this problem, the corresponding load value is achieved by summing the reaction forces of all the nodes along the base line of bulk materials or the substrate. The load versus displacement curves obtained from the FEM models are plotted in Fig.2.17 and Fig.2.18.

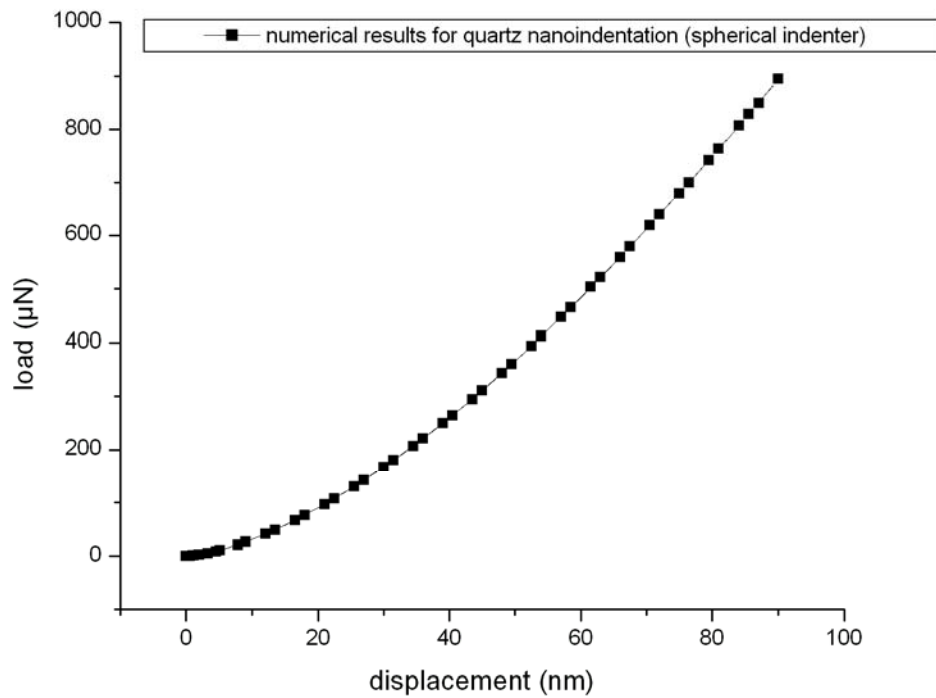


Fig.2.17. Load vs. displacement curve for model 1.

For models 1 and 3 the loading part of the load-displacement curve coincides with the unloading part due to pure elastic deformation of quartz, which completely recovers upon unloading.

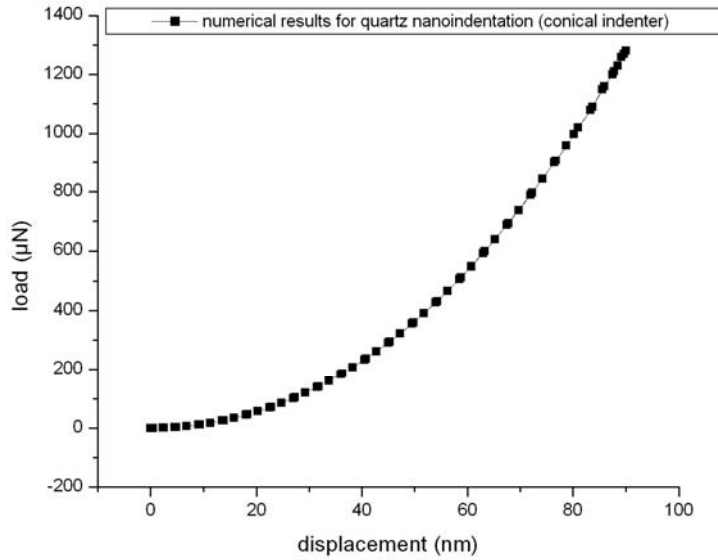


Fig.2.18. Load vs. displacement curve for model 3.

Fig.2.17 and Fig.2.18 show that the displacement for the elastic bulk quartz material during the indentation test is reversible.

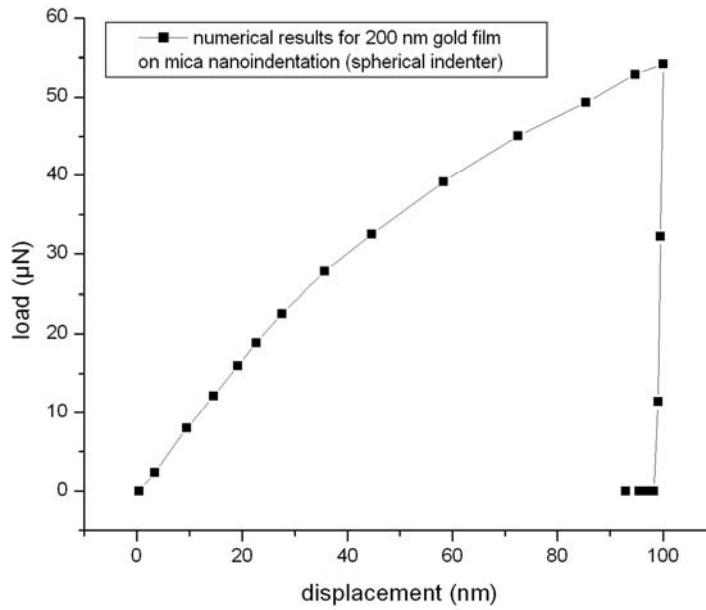


Fig.2.19. Load vs. displacement curve for model 2.

The load versus displacement curves in loading and unloading steps for models 2 and 4 are totally different. Fig.2.19 and Fig.2.20 show that the displacement for the elastic perfectly plastic gold film during the indentation test is irreversible. The load drops rapidly to zero during the unloading step. The indenter is free of contact after a short period of elastic deformation recovery of the film and the mica substrate.

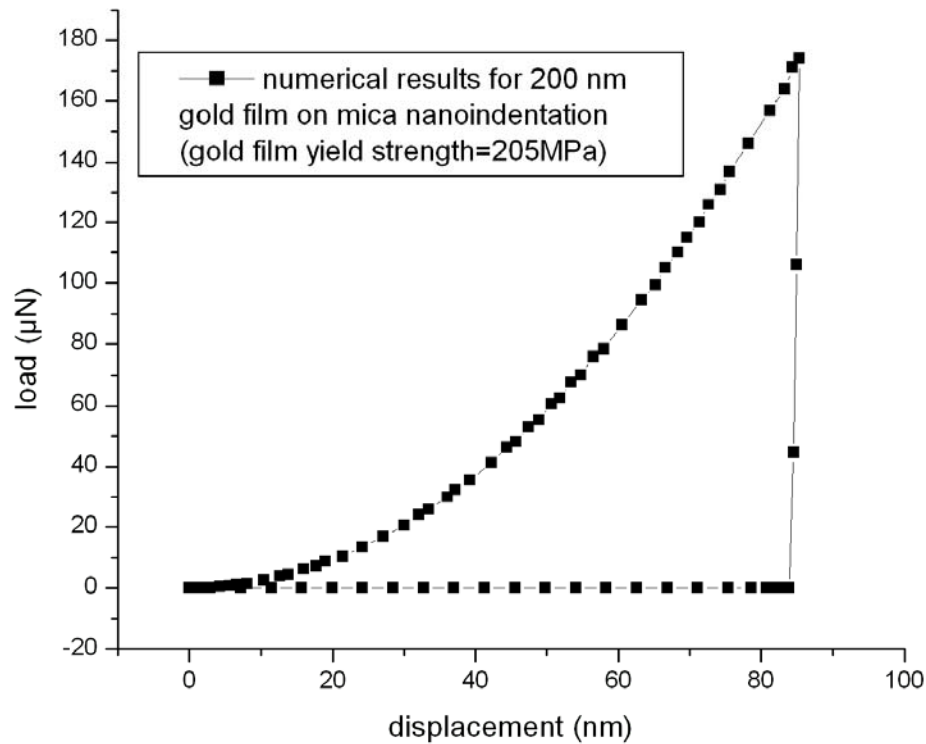


Fig.2.20. Load vs. displacement curve for model 4.

2.3.4 Comparison of Numerical Results and Experimental Data

To verify the accuracy of the results obtained from FEM simulations, nanoindentation experiments were conducted with a Triboscope Nanomechanical Testing System (Hysitron Inc., Minneapolis, MN). The indenter used for the experiment is the

three-sided pyramid Berkovich tip. The bulk material is quartz. The thin film/substrate materials are gold and mica. All the geometry parameters are the same as those in models 3 and 4. The maximum indentation depth is 90 nm for quartz and is 85.3 nm for the gold film/mica substrate. The comparisons of load versus displacement curves obtained from numerical results and experimental data are presented in Fig.2.21 and Fig.2.22.

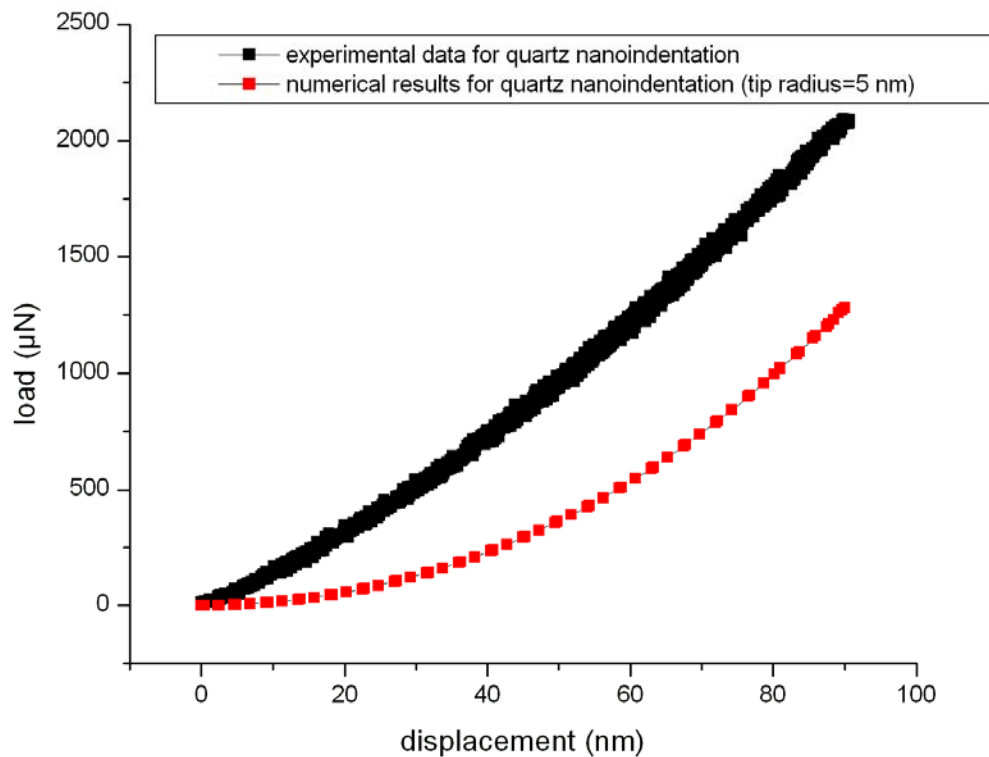


Fig.2.21. Comparison of numerical results and experimental data for model 3.

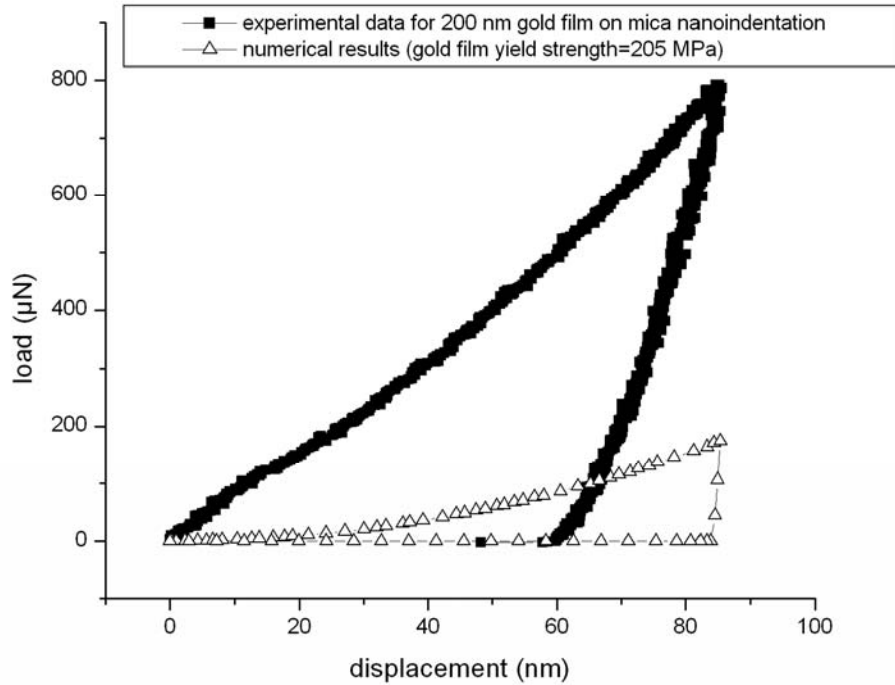


Fig.2.22. Comparison of numerical results and experimental data for model 4.

2.4 Discussion of Numerical Results

From the comparison of numerical results and experimental data presented in section 2.3.4, a disagreement appears. This may be caused by several reasons outlined below.

2.4.1 Effect of Tip Radius on the Simulation Results

Practically, a perfect indenter tip without the round end doesn't exist. In numerical analysis, a perfect indenter tip will cause stress singularity around the contact point. To get the nonlinear numerical analysis convergent, round tip of the indenter must be used. The tip radii are set to be 5 nm and 100 nm in models 3 and 4, respectively. This

artificial parameter may be different from the actual parameter of the Berkovich indenter used in the experiment.

Fig.2.23 shows the load-displacement curves obtained for varying indenter tip radius. The round tip radius has significant effect on the results. The numerical results are sensitive to the change of the tip radius for the conical indenter. The larger the tip radius, the higher the maximum load value is. When tip radius changed from 100 nm to 200 nm, the maximum load increased by 14%. The numerical results and experimental data exhibit a better match by increasing the tip radius in model 3. From the comparison one can estimate that the actual tip radius of the indenter used in the experiment may be higher than 200 nm.

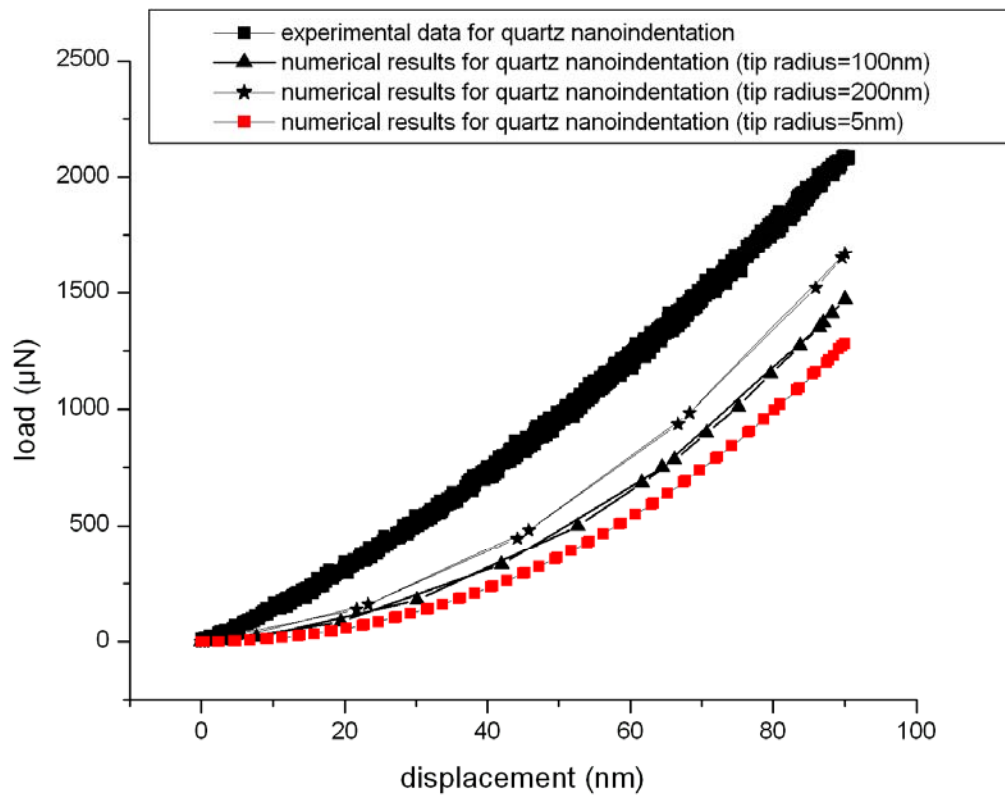


Fig.2.23. Effect of tip radius on the simulation results of bulk quartz nanoindentation.

2.4.2 Effect of Gold Film Yield Strength on Simulation Results

In previous studies [16, 22], lots of work had been done about tip radius effect. However, thorough discussion of the effect of materials mechanical properties on nanoindentation simulation is rare. Usually, the material properties used in numerical simulation are simplified. In this chapter, the material property of gold is assumed to be elastic-perfectly plastic with the yield strength of 205 MPa. However, the actual stress and strain relationship of this material is more complicated. Besides, yield strength of thin films can be much higher than that of the bulk materials [40, 41]. All these factors can affect the accuracy of numerical results.

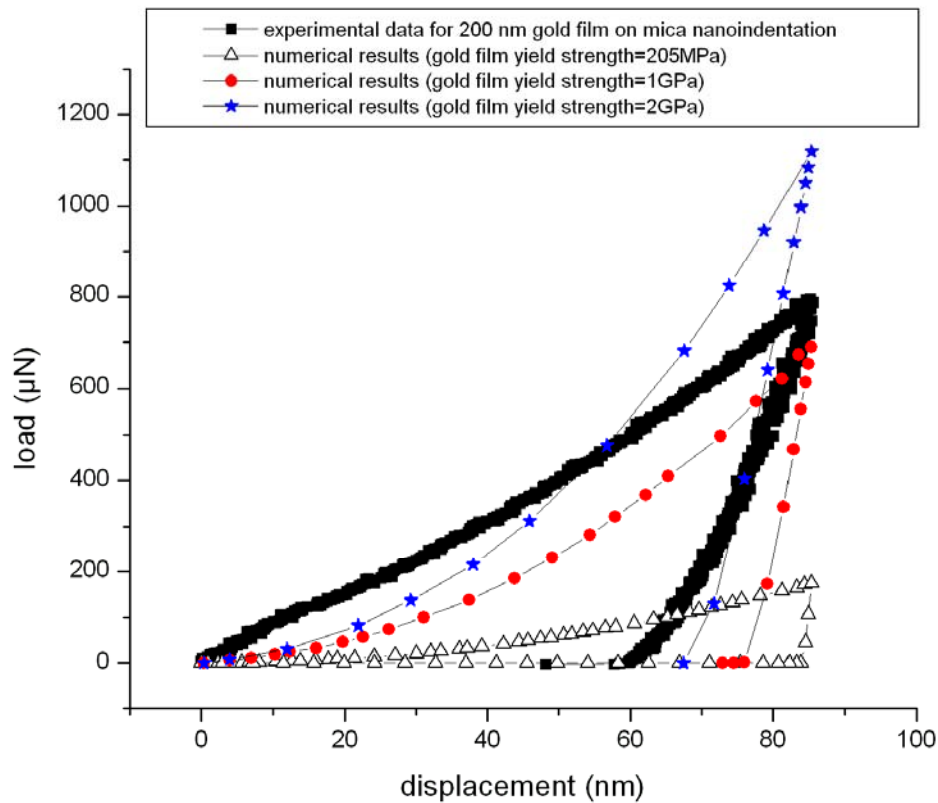


Fig.2.24. Effect of gold film yield strength on simulation results in model 4.

Fig.2.24 shows the effect of gold film yield strength on simulation results in model 4. With increasing yield strength of the gold film, the maximum load of numerical results increases, and both the loading and unloading parts of the curve can get closer to experimental data. The bulk gold yield strength 205 MPa is too small to be realistic in this simulation. When the value of yield strength changed from 1 GPa to 2 GPa, the maximum load increased by 62%. The numerical results demonstrated greater sensitivity to the change of gold film yield strength in model 4 than the change of tip radius in model 3. A perfect fit can be obtained given the appropriate yield strength value and the tip radius.

2.4.3 Other Factors Affecting the Accuracy of Simulation Results

Other than the two factors mentioned above, the selection of contact algorithm, the determination of contact element key options and other nonlinear parameters can affect the results. The determination of mesh density and other nonlinear parameters in FEM commercial software may have effect on numerical results. Coarse meshing can save computing time but may decrease the calculation accuracy. Fig.2.25 shows a good fit between the FE results and theoretical results from Hertz equations. This comparison reveals that the mesh density and the selection of the parameters in nonlinear calculation in this chapter are appropriate.

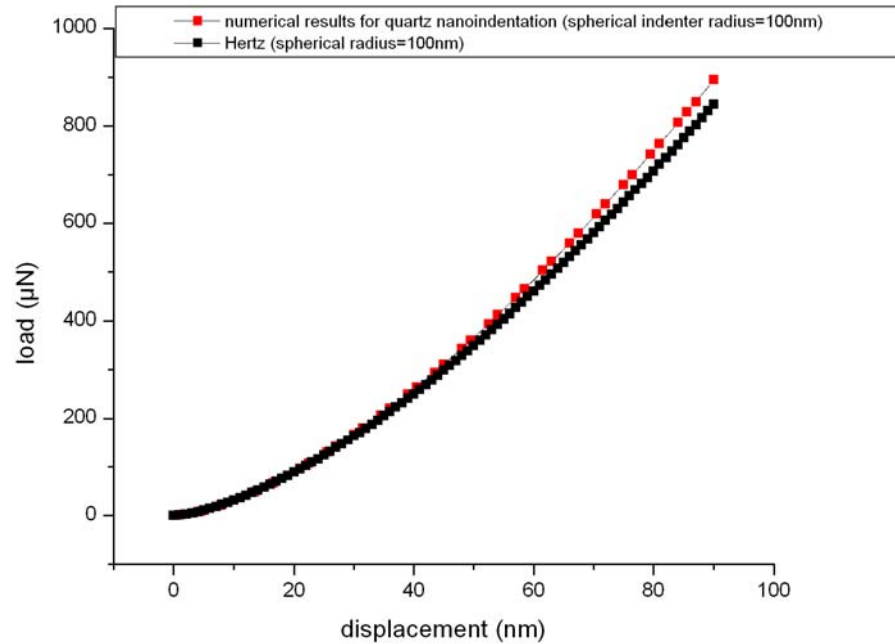


Fig.2.25. Comparison of numerical results and theoretical results for model 1.

2.4.4 Identification of Elastic-plastic Transition

To analyze the accuracy of the numerical results, the elastic-plastic transition through the gold film nanoindentation process should be identified. Fig.2.26 shows the comparison of FE results and theoretical results from Hertzian elastic contact equations with the same spherical indenter radius of 200 nm. Since the displacement of mica substrate is not taken into account, the loading curves of the Hertz results had overestimated a bit. From the figure one can see that for gold film indentation (yield strength=1GPa or 2GPa), the elastic-plastic transition occurs when indentation depth is less than 10 nm. Since the gold film with a yield strength equal to 205 MPa is so soft that the nanoindentation process goes into the plastic deformation from almost the beginning.

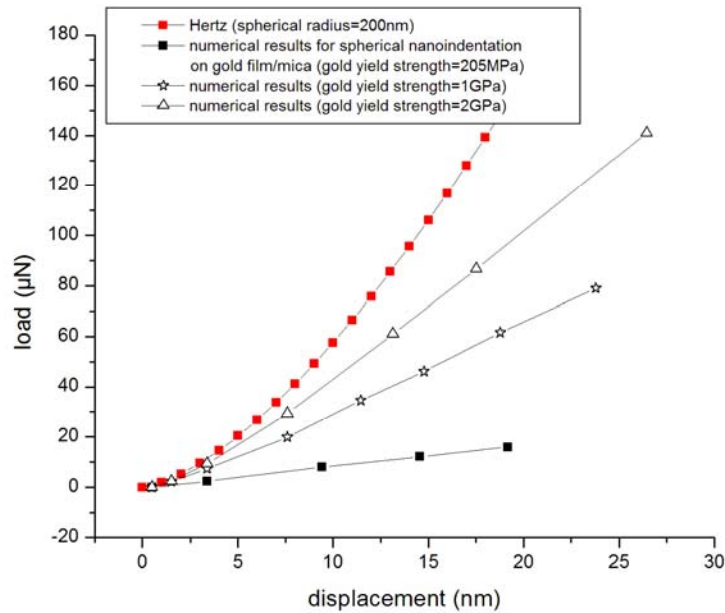


Fig.2.26. Comparison of FE results and theoretical results for model 2.

The conical indenters used in the FE models 3 and 4 have spherical cap due to the tip rounding. The height of the spherical cap is 5.85 nm and 11.70 nm for 100 nm and 200 nm tip radii, respectively. Within this range, Hertzian elastic contact equations for spherical indenter can be used for comparison with numerical and experimental data of conical nanoindentation.

Fig.2.27 and Fig.2.28 show this comparison. In Fig.2.28, the beginning of the loading part is enlarged. As mentioned above, the loading curves of the Hertz results had overestimated a bit. From the figures one can see that the elastic-plastic transition occurs when indentation depth is less than 5 nm. The experimental data in the beginning of indentation might be affected by the hard mica substrate, or the actual effective radius is larger, since the curve is higher than the Hertzian curve.

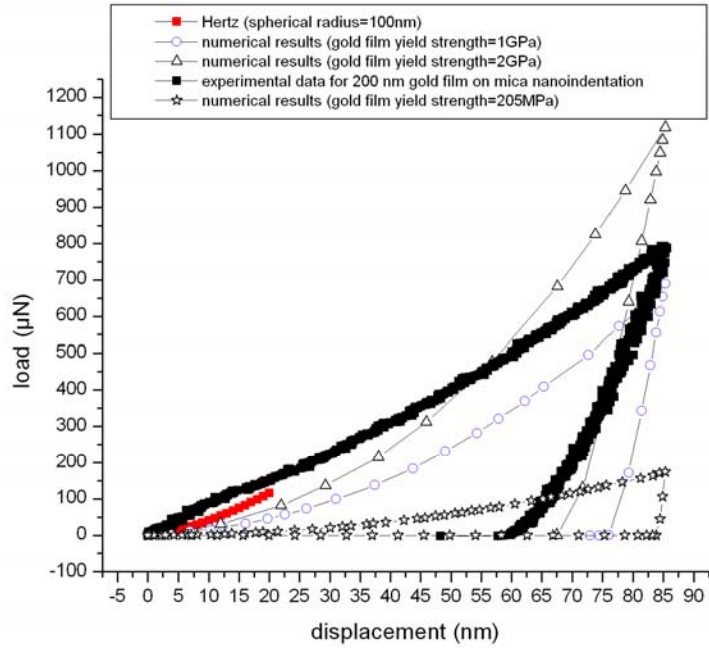


Fig.2.27. Comparison of theoretical, numerical and experimental data for model 4.

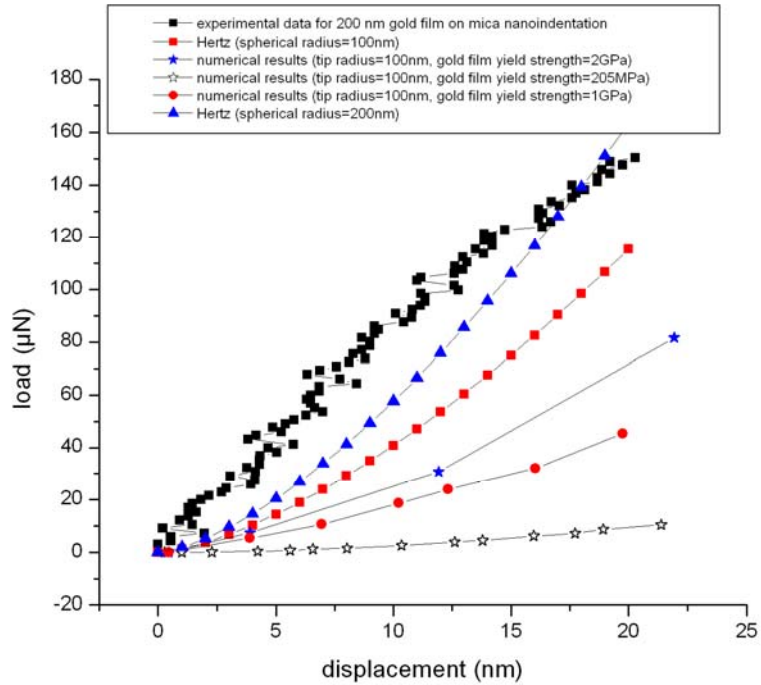


Fig.2.28. Comparison of theoretical, numerical and experimental data within the indentation depth of 20 nm for model 4.

2.5 Conclusions for Chapter 2

In this chapter, the finite element method was used to simulate the whole process of nanoindentation test. Two kinds of indenters, spherical and conical, were used to simulate indentation test of bulk material and thin film/substrate materials. The modeling procedures were introduced in detail. The agreement between the FE calculations and experimental results is satisfactory to some extent with appropriate geometry parameters and mechanical properties of specimen materials. The indenter tip radius and the yield strength of gold film have significant effect on the accuracy of simulation results. Further research is necessary to simulate nanoindentation with fewer limitations caused by simplified models and assumptions.

Chapter 3 Finite Element Analysis of Multiple Site Damage Bonded Repair Structures

3.1 Introduction

Multiple site damage (MSD) is typical for aged aircrafts and usually appears in a form of multiple cracks of varying length and direction. In aircraft structures, MSD cracks usually array along rivet holes in fuselage and wings. These cracks can greatly reduce the structure strength and lifetime, therefore compromise the flight safety. Multiple long cracks may have higher stress intensity than a single crack of the same length, thus they are more dangerous, as will be shown in this chapter. Bonded patch repair is an effective way to stop MSD, thus aircraft structures durability and damage tolerance can be increased.

Research of bonded composite aircraft repair began in the early 1970s [42]. Lots of work has been done on bonded composite repair structures with single crack from the standpoint of design, analysis and experiments [43, 44]. Mall and Naboulsi used a 2-D 3-layer FE model to simulate a plate with a crack, an adhesive layer with a patch as the repair structure [45]. Variation of the stress intensity factor (SIF) values of a crack in the plate before and after repair was analyzed. Effects of patch debonding on the SIF values were discussed. Besides, nonlinear factors were considered in bonded repair analysis [46]. The effects of geometry, size and adhesive layer parameters on the damage tolerance of repair structure were studied. However, 2-D FEM has some application limits. Although

it is simple and fast, it is not capable of assessing the SIF variation along the crack width. Seo et al. investigated fatigue crack propagation in the repair structure of a thick plate and obtained the crack tip SIF values with 3-D FEM [47]. Lee et al. used successive 3-D FEM to simulate fatigue crack propagation in the repair structure [48]. The 3-D FEM is more accurate in bonded repair structure analysis, but is computationally intense.

Much work has been done on bonded repair structures with a single crack. However, research of the repair structure with MSD is rare. In this chapter, finite element method was used on bonded repair of aluminum plates with multiple site damages. A 2-D 3-layer model technique was used to deal with the damage area. A typical aluminum plate with collinear twin cracks was considered as an example. The effects of relative position of the two cracks, patch size and patch thickness on stress intensity factors were studied.

3.2 Obtaining SIF of MSD Plate After Repair

In this chapter, a 2-D 3-layer FE model was used to simulate the cracked plate, the adhesive layer and the composite patch. In the model, the adhesive layer was simulated as elastic continuum instead of spring elements. A general purpose FEA package was used in the analysis along with the direct method to obtain the SIFs. This model is simple and fast to implement with an accuracy close to the 3-D FE analysis. In Naboulsi and Mall's 2-D 3-layer model [46], Mindlin plate elements were used to simulate the three layers, and the Modified Crack Closure Method (MCCM) was used to obtain the SIFs. Based on the assumption that the deformation variation is linear along the element thickness, the SIFs on the cracked plate free side had to be obtained by

interpolation [45]. While in reference [45] authors analyzed bonded repair structure with a single crack, in this chapter, bonded repair structure with multiple cracks is analyzed.

In linear elastic fracture mechanics (LEFM), the crack tips SIF values can be simply obtained with the FEM direct method. In the direct method stress or deformation near crack tips is obtained with FEM first, and then the crack tips SIF values are calculated based on the stress field. There are two direct methods commonly used, the displacement method with non-singularity elements and the stress method [49, 50]. The methods simple description is presented next.

3.2.1 Displacement Method

From the displacement near the crack tip area and the SIF relationship, a set of SIF values, K_1^* can be obtained from the node displacement calculated by FEM:

$$K_1^* = \frac{Eu}{4(1-\nu^2)} \sqrt{\frac{2\pi}{r}} \quad (3.1),$$

where E is the Young's modulus, ν is the Poisson's ratio, r and θ are the polar coordinates with an origin at the crack tip, u are displacements on the crack surface, respectively. Some nodes displacements are selected to produce the $K_1^* - r/a$ curve. In a small area, where $r/a \rightarrow 0$, K_1^* can change abnormally since the regular elements used are not able to reflect the crack tip singularity. In order to increase the calculation accuracy, the linear part of the $K_1^* - r/a$ curve can be extended to vertical K_1^* axis, making an intersection at $r/a = 0$. The axis intersection point yields the K_1 value.

3.2.2 Stress Method

Similar to the displacement method, K values can be obtained from the relationship between the crack stress field and the SIF:

$$K^* = \sigma_{ij} \frac{\sqrt{2\pi r}}{f_{ij}(\theta)} \quad (3.2),$$

where

$$\begin{aligned} f_{xx}(\theta) &= \cos\left(\frac{\theta}{2}\right) \left[1 - \sin\left(\frac{\theta}{2}\right) \sin\left(\frac{3\theta}{2}\right)\right] \\ f_{yy}(\theta) &= \cos\left(\frac{\theta}{2}\right) \left[1 + \sin\left(\frac{\theta}{2}\right) \sin\left(\frac{3\theta}{2}\right)\right] \\ f_{xy}(\theta) &= f_{yx} = \sin\left(\frac{\theta}{2}\right) \cos\left(\frac{\theta}{2}\right) \cos\left(\frac{3\theta}{2}\right) \end{aligned} \quad (3.3),$$

by substituting nodes stress values into equation (3.2). Similarly, extending linear part of the $K^* - r/a$ curve to $r/a=0$ yields the SIF value. Usually σ_{yy} is used at $\theta=0^\circ$ to obtain K .

3.3 FE Model of the Repair Structure

3.3.1 Basic Assumptions

A 2-D 3-layer FE model was used to simulate cracked aluminum plate, adhesive layer and composite patch layer. Variation of crack tip SIF in the plate before and after patch repair was obtained by FEM. Basic assumptions were made based on the actual conditions of bonded repair structure in order to simplify calculations:

-The cracked plate and the patch thickness are much smaller than their in-plane dimensions. The structure is deformed within the linear elastic conditions.

-The adhesive is an isotropic material, in which only shear deformations are considered. For the one-side repair, the out-of-plane bending caused by structural asymmetry is not considered.

-All adhesive areas are perfectly bonded.

3.3.2 FE Model Validation

The same material properties and geometry as those presented in [45] were used to verify the FE model accuracy and to analyze the repair performance of Boron/Epoxy composite patched repair. Presented model accuracy is verified by comparisons shown in Table.3.1. The obtained result is larger than the Sun's 2-D result [51], and is in-between the Sun's 3-D model [51] and the Chau's 3-D model results [52]; it is close to the Mall's result [45]. Based on this comparison the model presented here can reflect the actual structure conditions and satisfy the calculation accuracy requirements.

Table 3.1 Validation of the FE model.

Models	this chapter 2-D	Mall et al. 2-D [45]	Chau. 3-D [52]	Sun et al. 2-D [51]	Sun et al. 3-D [51]
Normalized SIF value $K = \frac{K_1}{\sigma_y \sqrt{\pi a}}$	0.564	0.570	0.481	0.536	0.612

3.3.3 Model Geometry and Materials Mechanical Properties

A 2-D 3-layer model is based on the aluminum plate geometry with collinear twin cracks. The specimen is made of 2024T3 aluminum alloy with the length of 200 mm, the width of 80 mm, and the thickness of 2 mm. Adhesive is FM73 epoxy with a thickness of 0.2 mm. Composite patch is made of Boron/epoxy laminate. The materials mechanical properties are presented in Table 3.2 (obtained from reference [53]).

Table 3.2 Materials mechanical properties [53].

Mechanical Properties	Aluminum plate	Adhesive layer	Boron/Epoxy
E_1 (MPa)	70000	1000	208000
E_2 E_3 (MPa)	-	-	25400
ν	0.32	0.32	0.17
G_{12} G_{13} (GPa)	-	-	7.2
G_{23} (GPa)	-	-	4.9

E =Young's modulus, G =Shear modulus, ν =Poisson's ratio; 1, 2, and 3 are the in-plane, transverse and out-of-plane transverse fiber directions, respectively.

The patch width in this model is the same as the plate width for comparison purposes, and the patch length is 40 mm. The model geometry is shown in Fig.3.1. The patch is bonded on one side of the plate and fully covers the cracks.

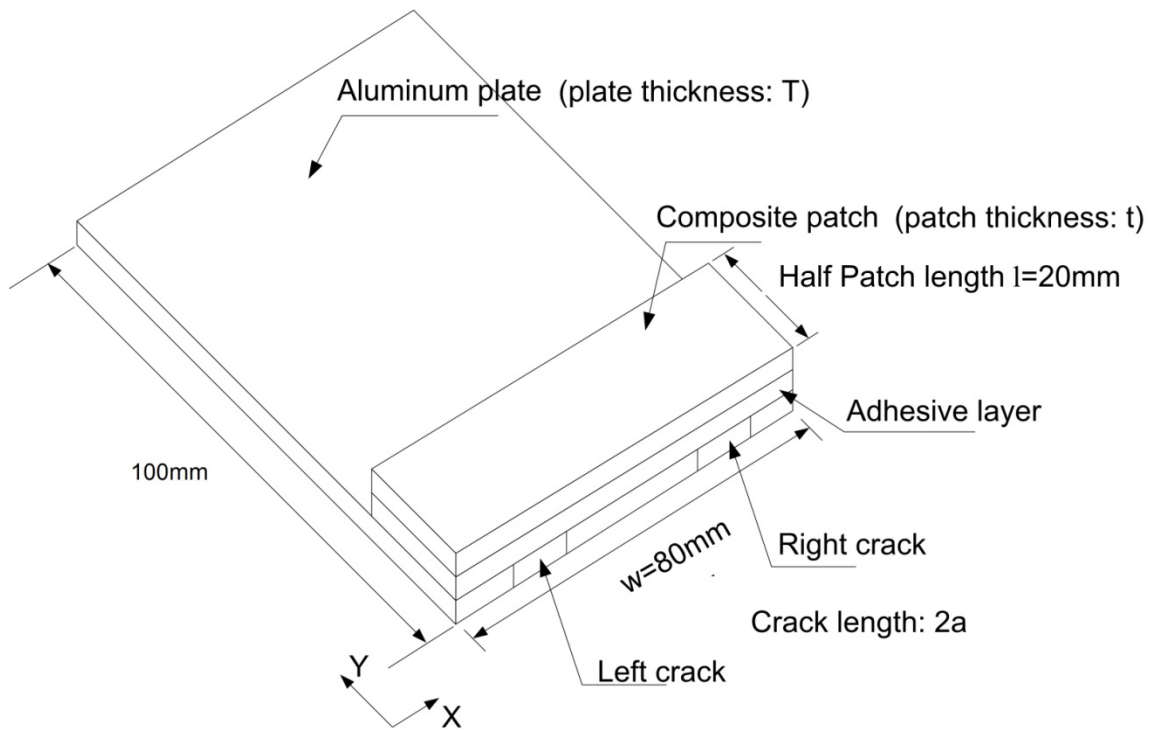


Fig.3.1. Schematics of the model geometry.

3.3.4 Boundary Conditions for Repair Structure

In this FE analysis, 4-node shell elements were used to simulate the cracked plate, the adhesive layer and the composite patch. The mesh density was higher near the crack tips. Only half of the structure was modeled due to its symmetry. One side of the model was added with symmetric boundary conditions, and the other side was added with the distributed load. Direct method was used to obtain the SIF values. Finite element mesh for the entire model and the crack tips is shown in Fig.3.2.

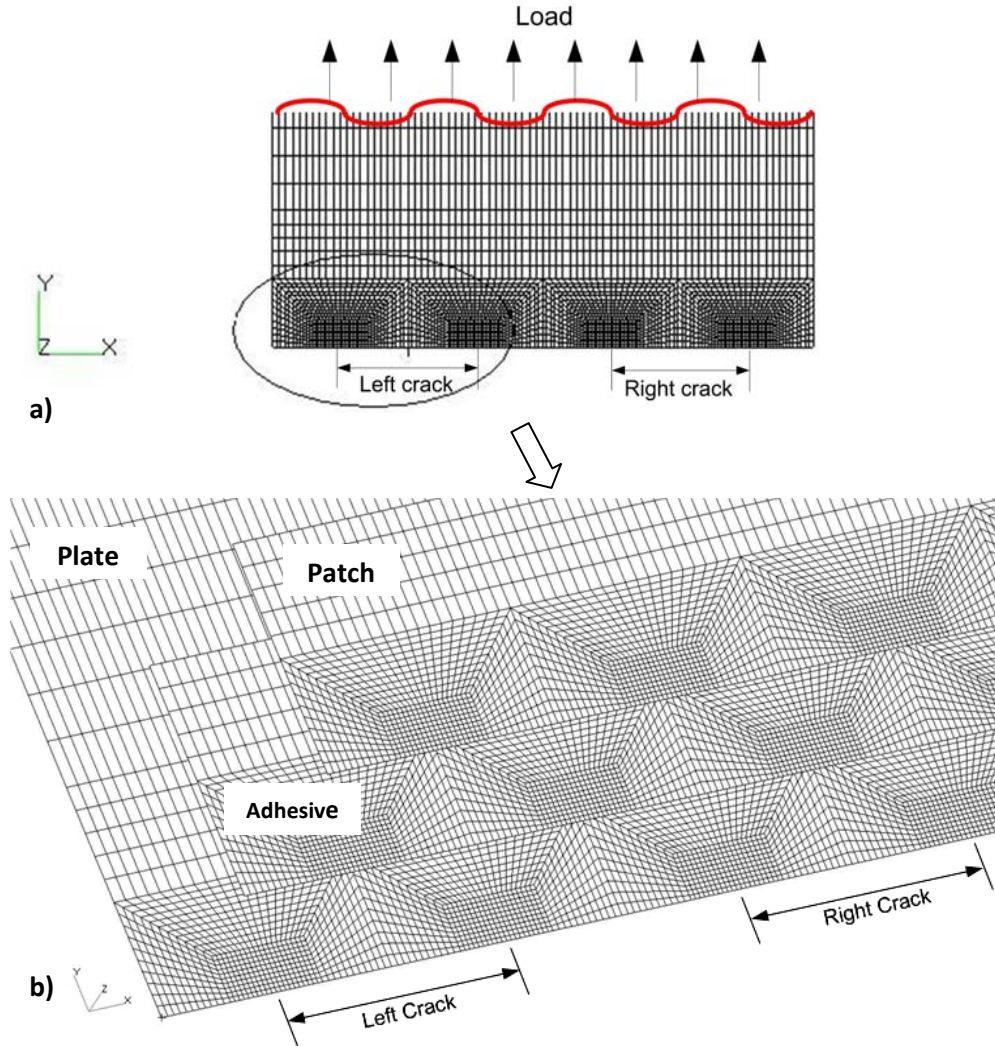


Fig.3.2. a) Finite element mesh of the entire model and b) the crack tips.

3.4. Results and Discussion of Repair Structure Simulation

3.4.1 SIF Variation With the Crack Length

Fig.3.3 compares the normalized SIFs of a single crack and twin cracks of different length. Stress intensity factors were normalized by $\sigma \cdot \sqrt{\pi a}$ (the stress times the square root of π times the half-crack length), and the crack length was normalized by the

plate width. In Fig.3.3, the normalized SIFs of the left crack tip A and the right crack tip B, as shown schematically in Fig.3.4, are plotted. SIFs of the single crack were obtained from handbook [54]. Calculation results show that compared with a single crack, collinear twin cracks have smaller SIFs for shorter crack length, and thus a single crack is more likely to propagate in this case. The SIFs for the twin cracks depend on the relative distance between those cracks and between the cracks and the boundary. When the distance between the tips of collinear twin cracks is about 50% of the distance between their centers ($d/D=50\%$, see Fig.3.4), the SIF values near the twin cracks tips are close to those of the single crack. After that, at larger crack length, $K_1(B)$ and $K_1(A)$ increase rapidly and exceed SIF values of a single crack, respectively. Twin cracks are more likely to propagate in this case compared with the single crack of the same length.

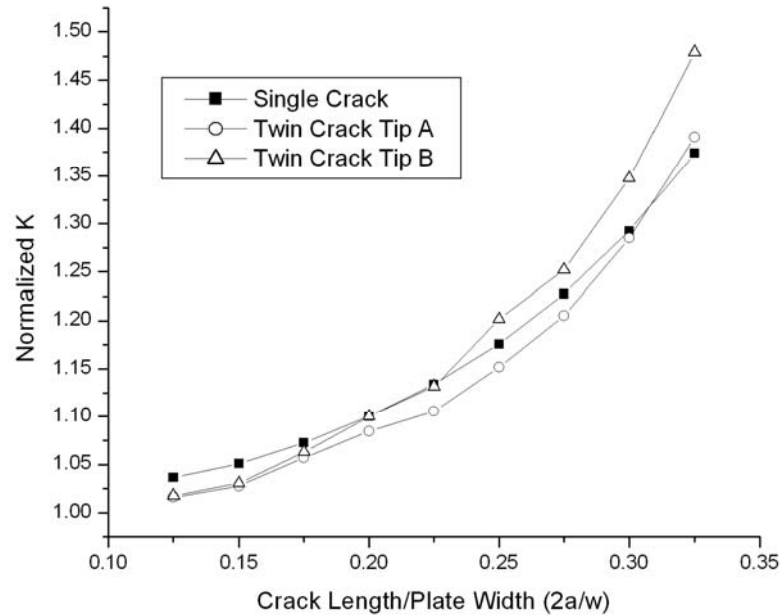


Fig.3.3. Comparison of the normalized SIFs values between a single crack and twin cracks of varying length. SIFs of the single crack were obtained from handbook [54].

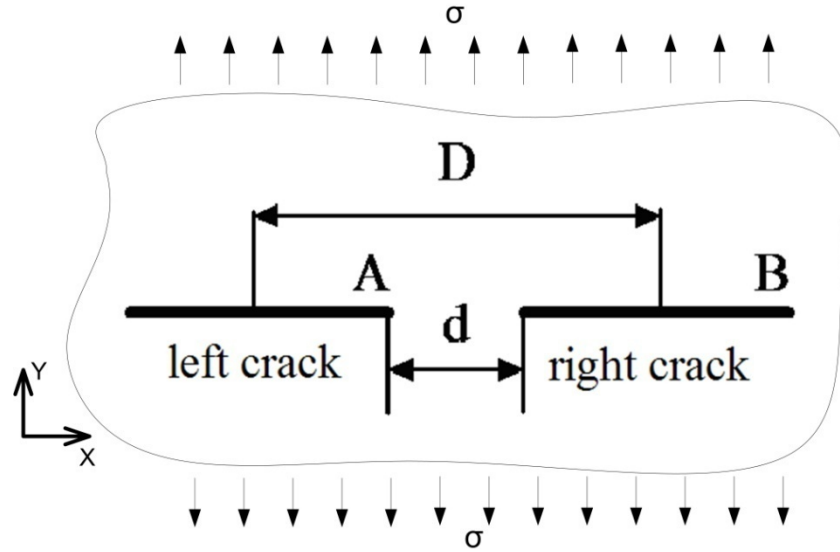


Fig.3.4. Twin cracks geometry configuration.

3.4.2 Patched and Unpatched Plates SIFs Variation With the Crack Length

Comparison of the SIF values between patched and unpatched twin cracks of different length is presented in Fig.3.5. Variation of SIF values shows that bonded repair with composite patch can greatly reduce SIF of collinear twin cracks. The longer the crack length, the higher the SIF reduction is. The difference between the SIF values of the A and B cracks in the unpatched plate increases with the crack length. Patch repair decreases the SIFs by over 90%, and after repair, there is almost no difference between the A and B cracks SIFs, signifying the repair efficiency.

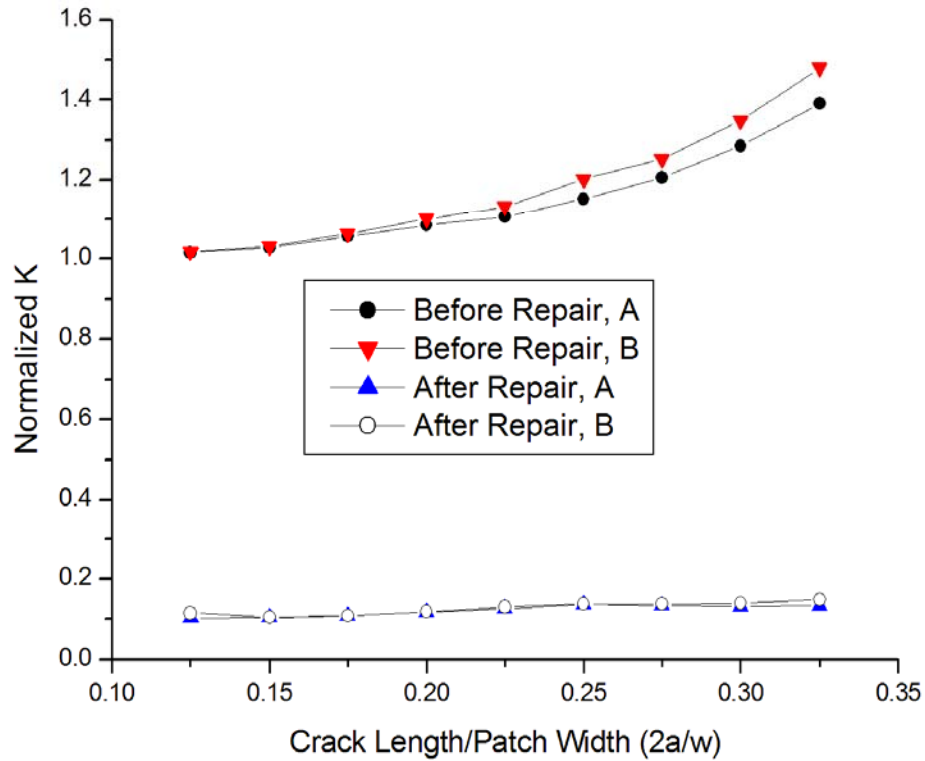


Fig.3.5. Comparison of the SIFs values between patched and unpatched twin cracks of varying length.

3.4.3 Patch Length Effect on the K Values

Consider a certain fixed crack length of $a=10$ mm, and then calculate the K value for A and B cracks after repair for varying patch length in the 2-D FE model. The results of this exercise are shown in Fig.3.6. With increasing patch length, the K value decreases so that the repair performance improves. However, when patch length reaches a certain value, the K value of the repair model increases and the repair performance declines. When the patch is small, increasing its length has a positive effect on the load transfer

from the cracked plate to the composite patch through an adhesive layer, thus releasing the load concentration near the crack tips. The repair performance declines when the patch length continues to increase and exceeds a certain length due to two effects. First, there is only a small adhesive layer area near the joint that can effectively transfer the load by shear deformation. In the longer part of the joint, the adhesive layer transfers less load by shear deformation. In the longer part of the joint, the adhesive layer transfers less load [55]. This situation makes a patch layer behave like a staple, which pulls the crack sides together. If the staple is too long or too short, it is less efficient in reducing the crack opening. Second, the local stiffness of the patched area in the cracked plate increases after repair so that the load transferred in the patched area increases. When the patch length is over seven to eight times the crack length, the SIFs tend to plateau (Fig.3.6). There exists an optimal patch length, 1.5-2 times longer than the crack length for which the SIFs are at a minimum, which guarantees the best repair performance.

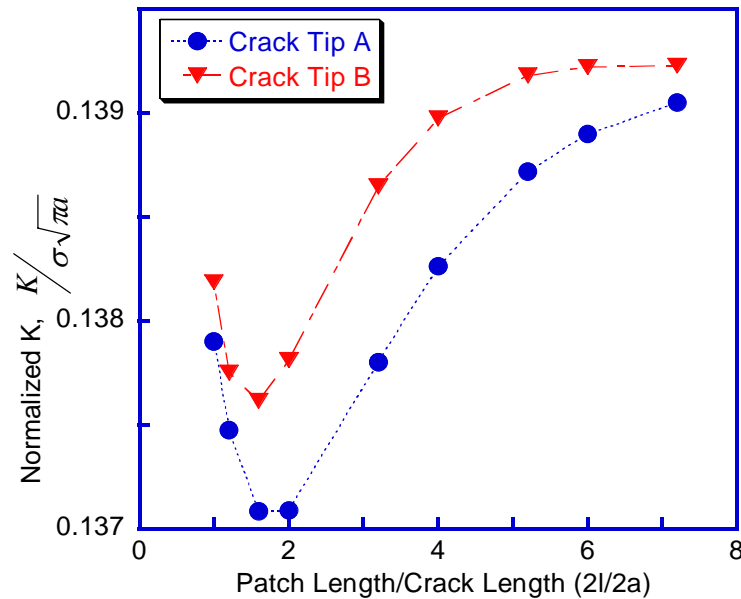


Fig.3.6. Effect of the patch length on the normalized SIF values of the repaired structure.

3.4.4 Patch Thickness and Layout Effects on the K Values

Consider the half crack length a of 10 mm, the patch thickness of 0.8 mm, and calculate the K value of the repaired cracked plate with 0° fiber layout, 90° fiber layout and $[0/\pm 45/90]_{2s}$ fiber layout, respectively. The comparison of these K values is presented in Table 3.3. The repair performance is relatively poor with the composite patch, whose 0° layout is along the x (crack) direction and is perpendicular to the applied load direction. The repair performance is the best for the composite patch, whose 0° layout is along the y loading direction. The repair performance of $[0/\pm 45/90]_{2s}$ layout is in-between the two cases presented above.

Table 3.3 Fiber layout effect on the SIFs.

Patch layout	0° layer is along the X direction	0° layer is along the Y direction	$[0/\pm 45/90]_{2s}$
Normalized SIF after repair	0.401	0.059	0.137

Fig.3.7 shows the patch thickness effect on the A and B crack tips stress intensity factors. With increasing patch thickness, the SIF for the patch repaired structure decreases, and the repair performance improves. However, when patch thickness continues to increase, the improvement of repair performance is limited. Besides, if the patch thickness is too large on one side of patch repair, the out-of-plane bending moment cannot be neglected causing a side effect on the repair performance. So the patch thickness needs to be optimized based on the actual loading conditions. As a general rule,

the patch thickness of 30-40% of the plate thickness will provide adequate decrease in K , based on Fig.3.7.

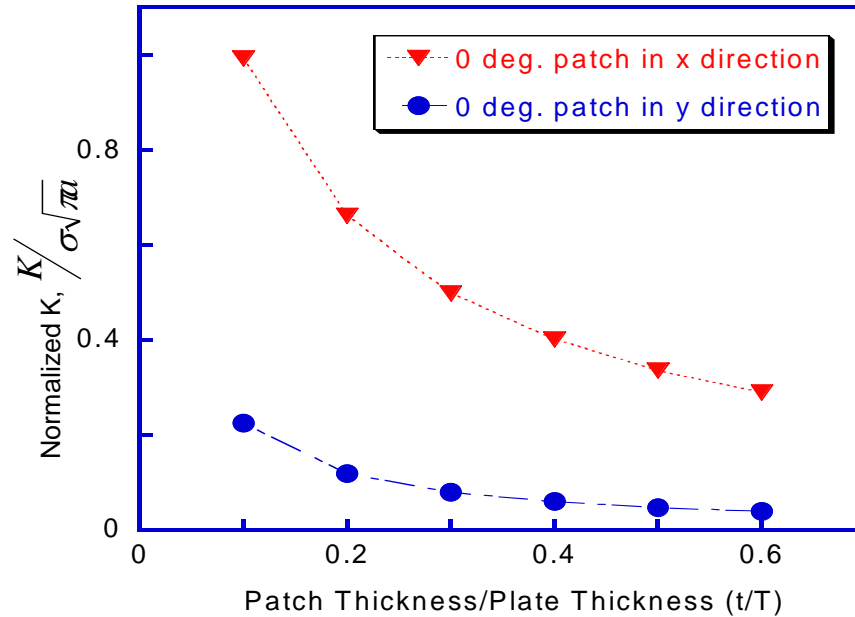


Fig.3.7. Patch thickness effect on the SIFs values of the repaired structure.

3.4.5 Patch Debonding

Debonding can occur around cracks due to fatigue [53]. Patch debonding can be more severe when applied load increases [56]. The size of debonded area has important effect on repair performance [57]. The larger the debond area is, the lower is the repair efficiency. Here, debonding can be simulated by releasing the node constraint between the adhesive layer and the aluminum plate. The approximate reduction of repair efficiency can be 80% in case of full width debonding when the debonded area reaches 50% of the patch area.

In addition, one has to consider thermal and environmental effects that can lead to patch debonding. Temperature cycling can also cause fatigue interfacial cracks. Patch debonding can also be induced due to environmental effects, where moisture substantially reduces patch adhesion. Trapped at the interface, moisture turns into ice in flight, loading and propagating interfacial defects that turn into interfacial cracks.

3.5 Conclusions for Chapter 3

2-D 3-layer FE model can be used to calculate the SIFs of collinear twin cracks. The relative position of collinear twin cracks has significant effect on the crack tip SIFs in certain stress fields. When the distance between the tips of collinear twin cracks is larger than between their centers, the SIF can be calculated as for the single crack. In this condition, the obtained SIF is conservative. When the distance between the collinear twin cracks tips is less than between their centers, the SIF of twin cracks will exceed that of the single crack, requiring repair. MSD is worse than a single crack, and definitely needs to be repaired.

The stress intensity factors at the tips of collinear twin cracks can be reduced by over 90% through bonded composite repair. The longer the crack, the better the repair performance is. However, for certain cracks and stress fields, parameters like the adhesive properties, the patch length and thickness must be optimized in order to obtain the best patch repair performance. Patch length needs to be 1.5-2 times the crack length to minimize the SIF of the MSD. Large than needed patch size and thickness are not beneficial. Patch debonding should be controlled to a limited area.

Chapter 4 Thermo-mechanical Analysis of Porous Coatings on Steel for Catalysis

Applications

4.1 Introduction

A micro reactor or a micro channel reactor is a kind of device in which chemical reactions can take place in a confinement with typical lateral dimensions below 1 mm. The most typical form of such confinement is micro channels [58]. As micro reactors, micro channels can provide many advantages over conventional scale reactors, such as vast improvements in reaction speed, energy efficiency and yield, safety, reliability, scalability, on-site/on-demand production. Besides, they can provide a much finer degree of process control. Micro channels may be a valuable tool in the area of catalysis reaction in chemical engineering field. Since the gases passing through the micro channels are usually with a high temperature, the thermo-mechanical properties of micro channels should be investigated.

Fig.4.1 is the planar view of the coated micro channel plate specimen. The plate is made of steel 1.4301 [59]. The porous catalyst coating is made of porous SiO₂. There are three parallel micro channels on the top surface of the plate. The channel's length is 9.6 mm.

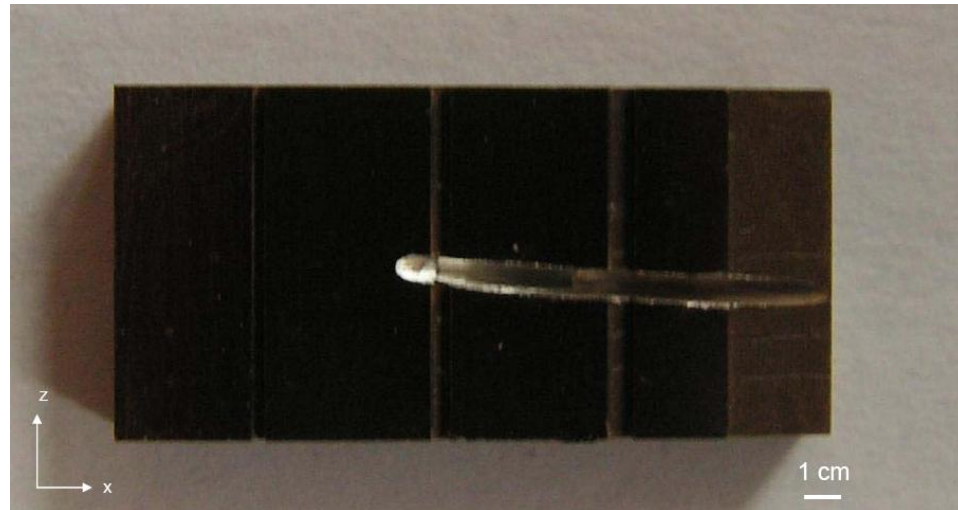


Fig.4.1. Planar view of the coated micro channel plate specimen.

Fig.4.2-4.4 are the optical images of the micro channel's profiles. The widths at the top are 0.3, 0.5 and 0.7 mm, respectively. The depths of all the three micro channels are 0.3 mm. The white substance in the channels is PMMA latex. These images show the actual geometry of the micro channels' profiles.

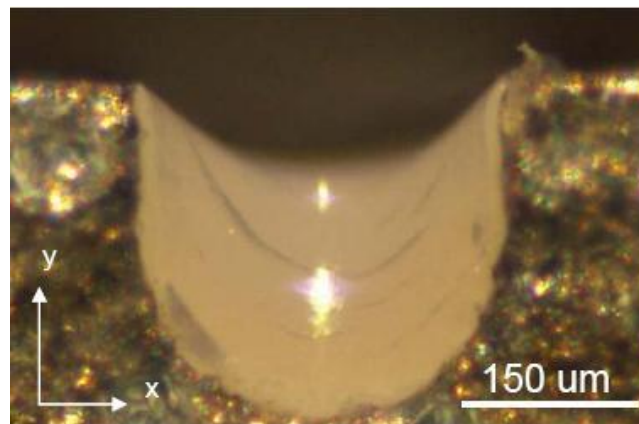


Fig.4.2. Cross-sectional optical image of 0.3×0.3 mm micro channel's profile. These micro channels were manufactured in the Leibniz Institute for Catalysis in Berlin, Germany in Dr. Ralph Kraehnert Group.

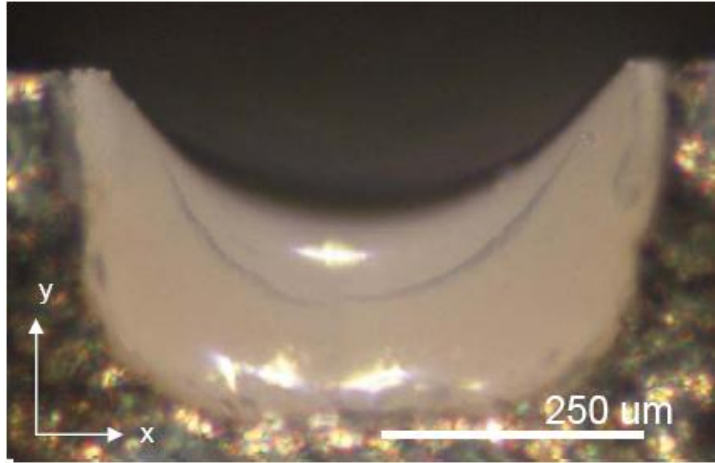


Fig.4.3. Cross-sectional optical image of 0.5×0.3 mm micro channel's profile.

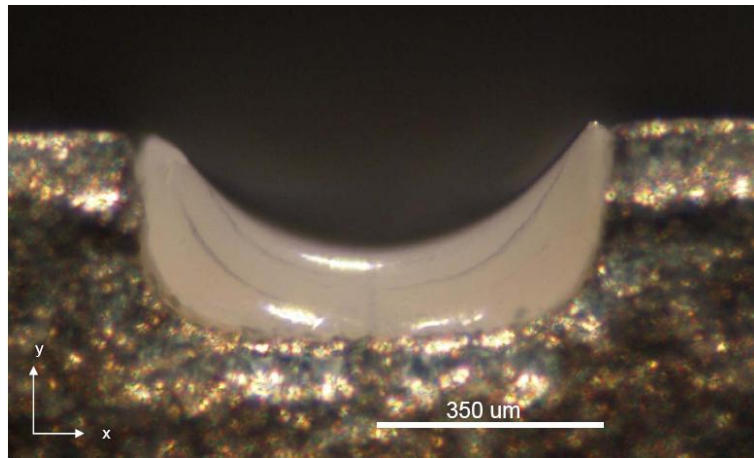


Fig.4.4. Cross-sectional optical image of 0.7×0.3 mm micro channel's profile.

4.2 Mechanical and Other Properties of the Film/Substrate Structure

Table 4.1 summarizes mechanical properties of materials used in the micro channel system. Porous SiO₂ film has lower thermal expansion coefficient than steel, thus will be under tensile stresses upon heating.

Table 4.1 Mechanical and thermal properties of the film and the substrate [59-63].

Mechanical Properties	Porous film coating	Steel substrate
E (GPa)	73	200
ν	0.17	0.3
α (1/°C)	0.5e-6	18e-6

E =Young's modulus, ν =Poisson's ratio, α =linear thermal expansion coefficient.

4.3 Problem Description

The films were deposited on the steel substrate by dip coating. Deposited materials accumulated at the lower end of the micro channels due to gravity, making the films thicker at the bottom. Then during the heating process, the temperature was increased up to 500 °C. Cracks were found mainly at the lower end of the micro channels, where film thickness is higher. To obtain the root causes for the thick film cracking, finite element models were used to analyze the intensity and distribution of film stress.

4.4 FEM Modeling of Micro Channel/Film Thermo-mechanical Deformation

4.4.1 Basic Assumptions

A 2-D FE model was used to simulate the coated micro channel plate. Variation of thermal stress and thermo-mechanical deformation after the 500 °C temperature increase was obtained by FEM. Assumptions were made based on the actual conditions of film/substrate structure in order to simplify calculations:

-The porous coating film and the steel substrate are isotropic materials. All deposited areas are perfectly bonded.

-The structure is deformed within the linear elastic conditions through the heating process.

-The 2-D models are built based on the cutoff profiles of coated micro channel plate. All the models are in the condition of plane strain.

-Heating process may cause in and out-of-plane plate curvature due to the thermal expansion mismatch of the film and the substrate. It is not considered in the numerical model. The displacement of the bottom surfaces are set to zero.

4.4.2 Model Validation

The dimension of the steel substrate used in local model is about 20 times of the thickness of the coating film. The difference between the local model and the full scale model is less than 2%. Based on this comparison the local model presented here can reflect the actual structure conditions and satisfy the calculation accuracy requirements.

4.4.3 Element Type and Boundary Conditions

In the FE analysis, 4-node solid elements were used to simulate the porous coating and the steel substrate. The mesh density was higher on the film and near the interface of the film/substrate. Due to the symmetry, only half of the structure was modeled. Left side of the model was added with symmetric boundary conditions, and the bottom side was added with constraint on the y direction. Temperature load was added to

the whole structure area directly. Finite element mesh for the 0.3×0.3 mm profile model is shown in Fig.4.5.

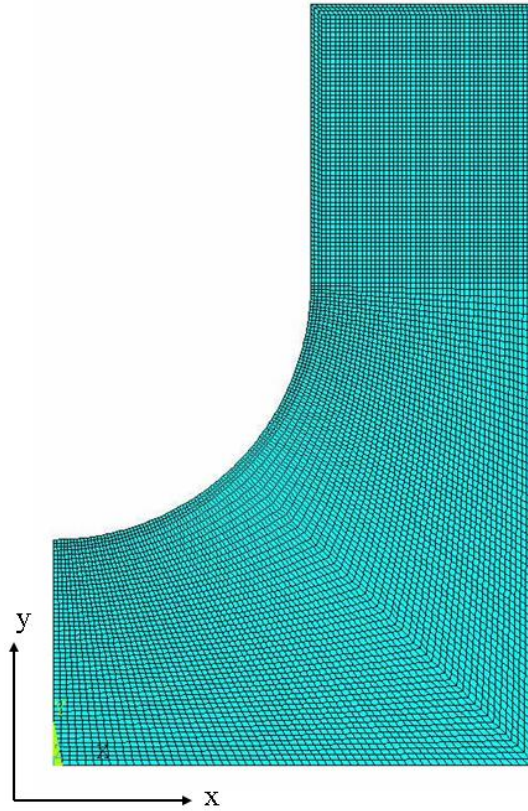


Fig.4.5. Finite element mesh for the 0.3×0.3 mm profile model.

4.5 Results and Discussion of Coatings in Micro Channels

4.5.1 Stress Variation With the Film Thickness

Since there was no experimental data to set the failure criteria for porous coating, stress in the coating film can be employed to investigate the root cause of the fracture. The cracks may tend to occur at the positions where stress value is high. Fig.4.6 shows

the stresses in x direction at the center bottom of the 0.3×0.3 mm micro channel profile as a function of the film thickness.

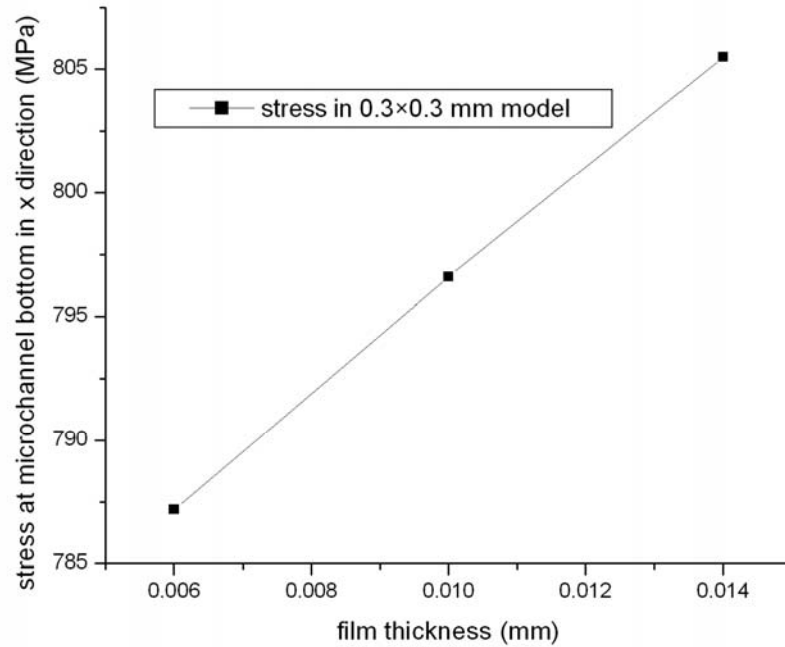


Fig.4.6. Effect of the film thickness on the stress at the micro channel bottom in x direction (0.3×0.3 mm).

Results in Fig.4.6 show that the stress in x direction at the center bottom increases with the film thickness. Fig.4.7 shows that the stress in y direction at the micro channel side wall decreases with the increasing film thickness.

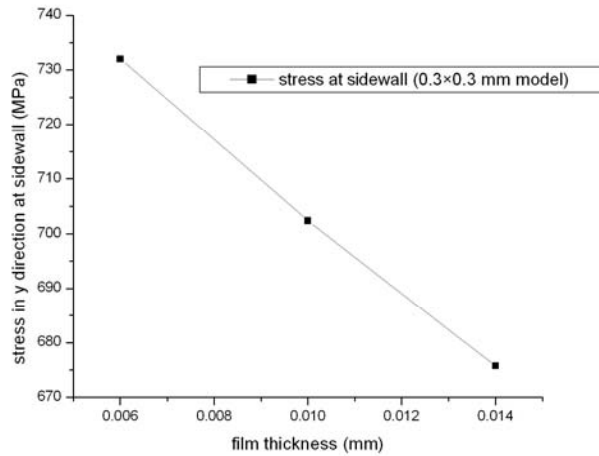


Fig.4.7. Effect of the film thickness on the stress at the micro channel side wall in y direction (0.3×0.3 mm).

In order to investigate the stress at the similar positions in different profile geometry, the stresses in the x direction at the bottom center of the 0.5×0.3 mm micro channel profile were obtained.

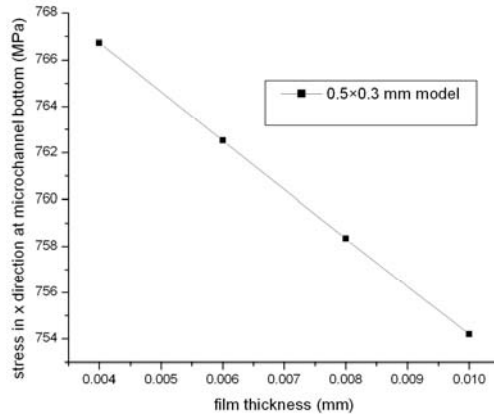


Fig.4.8. Effect of the film thickness on the stress at the micro channel bottom in x direction (0.5×0.3 mm).

The trend shown in Fig.4.8 is different from that for the 0.3×0.3 mm profile. The stress decreases with the increasing film thickness. However, variation of the stress at the side wall in 0.5×0.3 mm profile is similar with that in 0.3×0.3 mm profile, as shown in Fig.4.9.

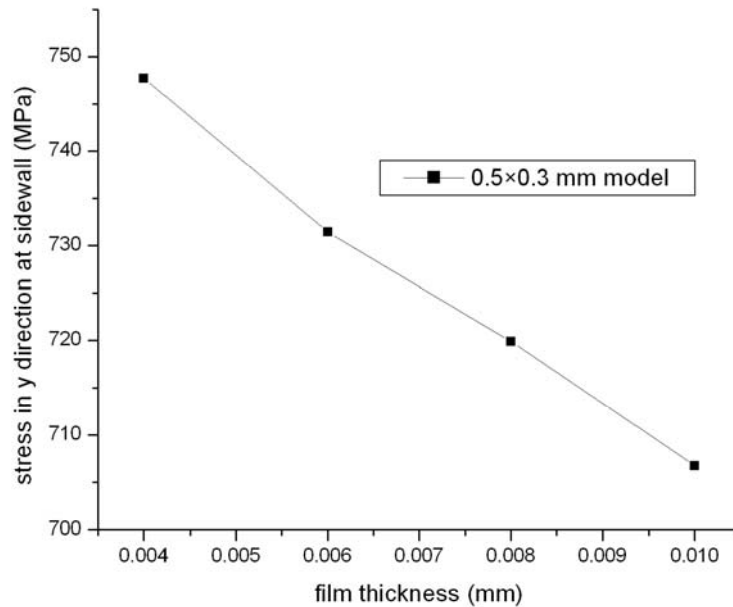


Fig.4.9. Effect of the film thickness on the stress at the micro channel side wall in y direction (0.5×0.3 mm).

Next, stresses at similar positions in 0.7×0.3 mm profile were obtained. The variation of stresses shown in Fig.4.10 is the same as that in the 0.5×0.3 mm profile.

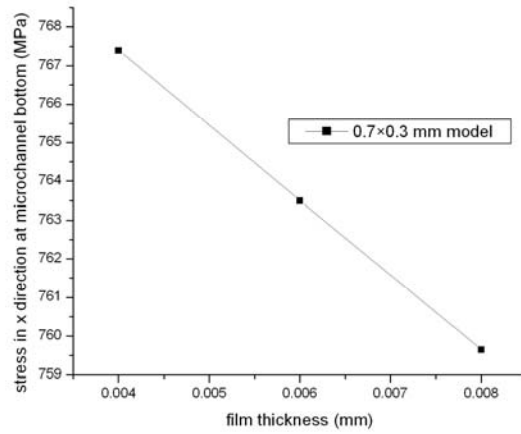


Fig.4.10. Effect of the film thickness on the stress in x direction at the micro channel bottom (0.7×0.3 mm).

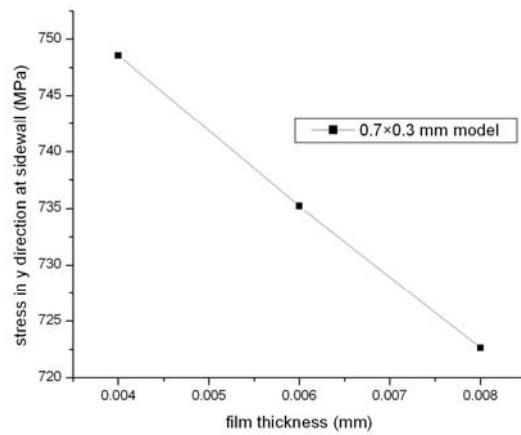


Fig.4.11. Effect of the film thickness on the stress at the micro channel side wall in y direction (0.7×0.3 mm).

There are many factors which will affect the variation of stresses with the increasing film thickness. On the one hand, the tensile stresses are applied to the thin film

from the substrate at the interface since the expansion of the substrate is much larger than that of the film. The stresses in the film caused by the tension will not distribute uniformly along the film thickness. It is reasonable that stresses on the top surface of the film will be smaller than those near the interface.

On the other hand, displacement mismatch due to thermal expansion mismatch between two materials will cause curvature in and out-of-plane. However, the finite element models established in this chapter assume that the bottom surface of the whole plate is completely constrained. This will cause bending moment on the plate top surface. Thus, the stresses caused by bending moment are larger at the top surface of the film than near the interface.

It is difficult to determine which factor weighs more. The ambiguous trends shown in the figures above cannot reveal the whole picture of the stress variation with the increasing film thickness. Stresses along a path rather than those at particular positions should be investigated.

4.5.2 Stress Distribution Along the Path

Consider a path starting from central bottom of the channel profile and ending near the upper point of the side wall. The principal stresses of the nodes along the path can be obtained using FEM. The thin films are made of brittle materials, so the principal stress can be seen as a kind of universal characteristic for comparison [24, 25]. From Fig.4.12 one can see the 1st and 2nd principal stresses distribution along the path for 0.3×0.3 mm model. Since the 1st principal stress is tensile and the values are much higher

than the 2nd principal stress values, in the following analysis only the 1st principal stress is employed.

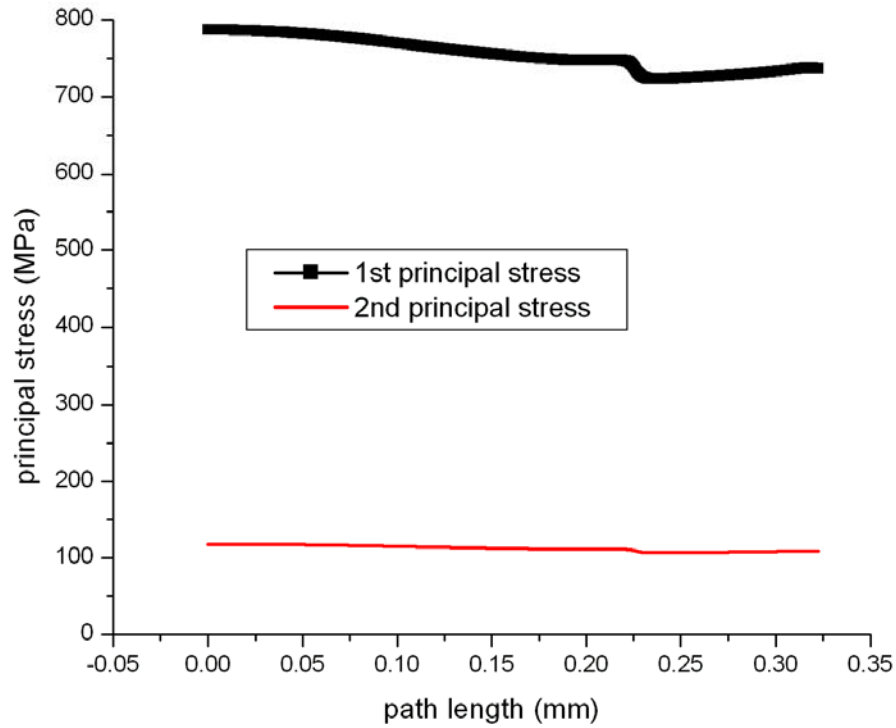


Fig.4.12. The 1st and 2nd principal stress distribution along the path.

Fig.4.13 shows the 1st principal stress distribution along the path with different film thickness for 0.3×0.3 mm model. In this case, principal stress at the channel bottom center reaches the maximum value. The maximum stress value increases with the film thickness.

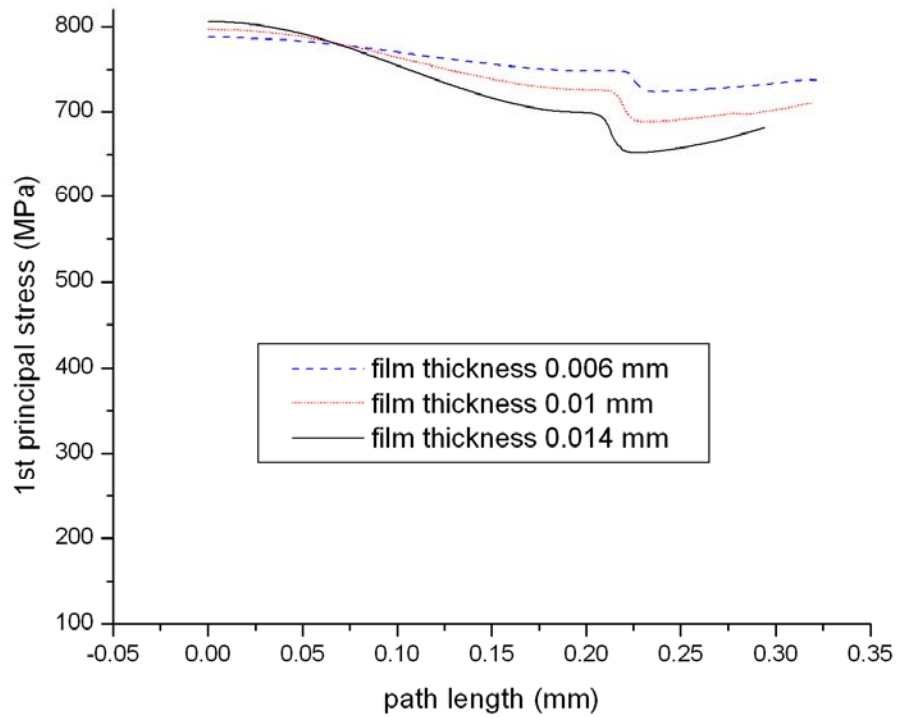


Fig.4.13. The 1st principal stress distribution along the path with different film thickness (0.3×0.3 mm).

Fig.4.14 shows the 1st principal stress distribution along the path with different film thickness of the 0.5×0.3 mm model. For this model, the maximum stress value occurs near the area between the flat profile's bottom and the round corner. With increasing film thickness, the maximum stress value increases.

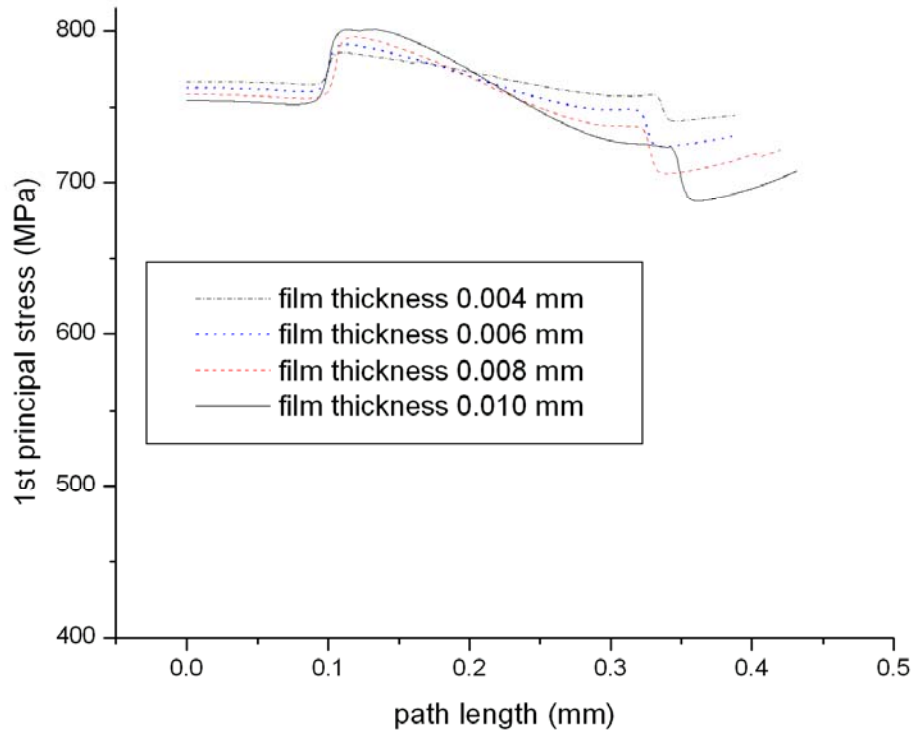


Fig.4.14. The 1st principal stress distribution along the path with different film thickness (0.5×0.3 mm).

Fig.4.15 is an SEM image of cracked 0.5×0.3 mm micro channel lower end (Image courtesy of Dr. S. Sokolov from Leibnitz Institute of Catalysis, Berlin Germany). Cracks concentrate at the round corner. The numerical analysis results are in good agreement with the actual fracture condition.

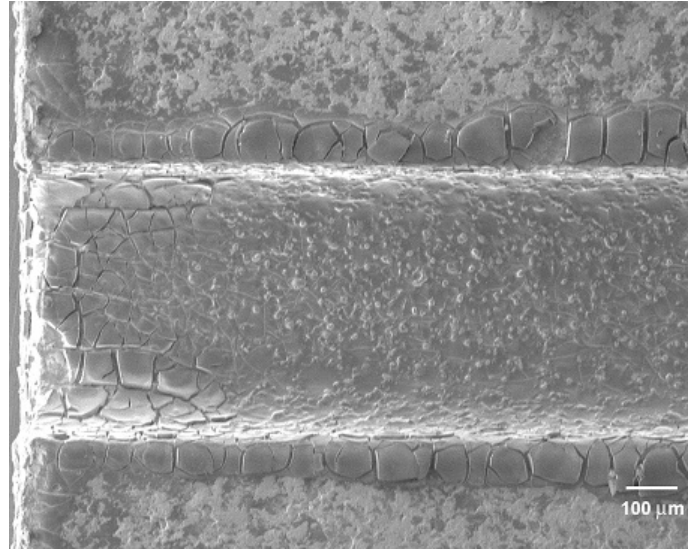


Fig.4.15. SEM image of cracked 0.5×0.3 mm micro channel lower end.

Fig.4.16 shows the 1st principal stress distribution along the path with different film thickness of the 0.7×0.3 mm model. The trend is similar to the 0.5×0.3 mm model. The numerical analysis results are also in good agreement with the actual condition, seen in Fig.4.17.

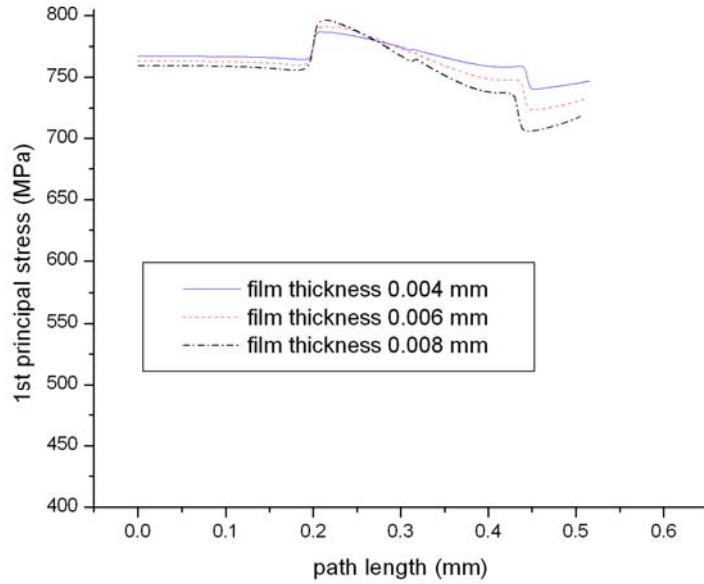


Fig.4.16. The 1st principal stress distribution along the path with different film thickness (0.7×0.3 mm).

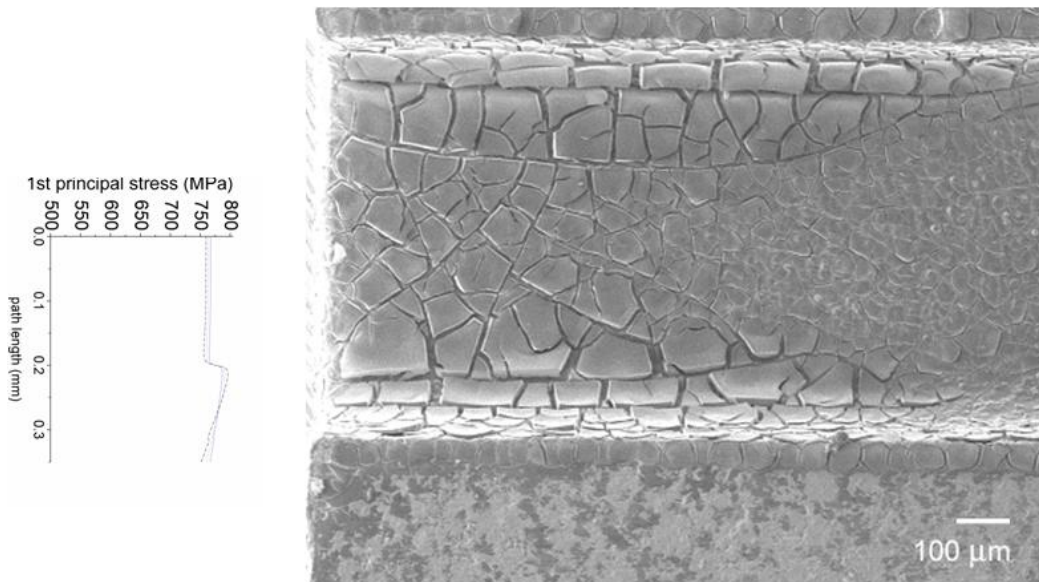


Fig.4.17. Comparison between FE results and the SEM image of cracked 0.7×0.3 mm micro channel lower end.

4.5.3 Process and Geometry Optimization to Avoid Failures

From the comparison, stress distribution in micro channel profiles with round corner is much smoother than in those profiles with the right angle. The maximum stress also decreases for the round corner profile. It is an effective way to optimize the profile geometry by an area fillet. Fig.4.18 shows stress distribution along the path with the same film thickness in different models. For the same film thickness, there is no significant difference between the maximum principal stress values in the three kinds of micro channel models.

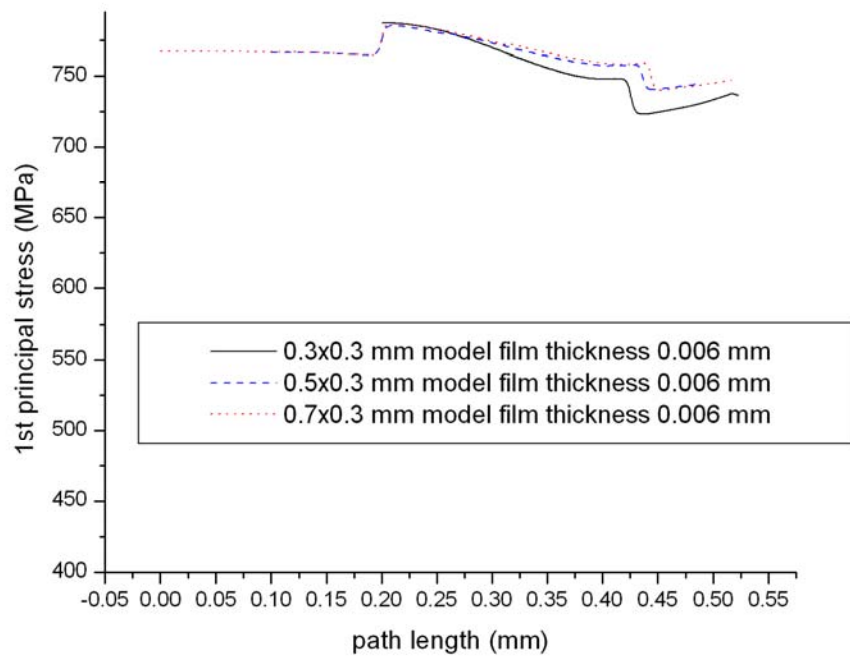


Fig.4.18. Stress distribution along the path with the same film thickness in different models.

4.5.4 Proper Materials Selection

It is obvious that the less the difference between the thermal expansion coefficients of the film and substrate, the less expansion mismatch between the film and the substrate is. One could possibly change the porous film properties to minimize the thermal mismatch stress.

4.5.5 Strain Estimation

From Fig.4.16 and Fig.4.17, elastic strain in x direction of micro channel profile can be obtained through measurement of image pixels. The pixel calculated strain is between 2 to 3 percent for both 0.5×0.3 mm and 0.7×0.3 mm profiles. This value is larger than FEM result which is 1.1 percent. One possible reason is that the phase transformation occurred in the film during the heating process [64, 65].

This is the first step to identify the cracking root cause to see how it is related to the stress concentration through mechanical thermal loading. 2-D FEM can provide a good prediction of the cracks location.

4.6 Conclusions for Chapter 4

In this chapter, finite element method was used for thermo-mechanical analysis of porous steel coatings on micro channels. Thermal stresses in the micro channels due to temperature changes were obtained. The effects of micro channel geometry on thermal stresses were studied in detail. The results revealed that in order to increase the mechanical performance of the coatings, film thickness and profile geometry must be optimized accordingly.

Chapter 5 Summary and Future Work

This work consists of three parts. The first part (Chapters 1 and 2) introduced basic procedures of nanoindentation simulation using finite element method. The relationship between load and indentation depth was obtained. The agreement between the numerical results and experimental data was satisfactory to some extent. It was shown that FEM is an effective tool for simulation of metallic films nanoindentation test. However, limitation caused by simplification of models and assumptions should not be neglected. With the rapid development of nano-scale mechanics and new numerical analysis methods, nowadays 2-D finite element modeling cannot meet the requirement of precisely simulating nanoindentation testing. In future work, advanced methods such as molecular dynamics should be employed to simulate the complex indentation process in nano length scale [66-68].

In Chapter 3, a 2-D 3-layer finite element modeling technique was used to analyze the bonded repair structure. The effects of relative position of two cracks, patch size, patch thickness on stress intensity factors were studied in detail. The results revealed that the stress intensity factors at the tips of collinear twin cracks can be reduced greatly through bonded composite repair. In order to increase the performance of the patch repair, the adhesive properties, the patch length and thickness must be optimized. In future work,

3-D simulation and theoretical analysis are needed to analyze the problem in practice without the simplified assumptions [69, 70].

In Chapter 4, finite element method was used for thermo-mechanical analysis of porous coatings in steel micro channels used for catalysis. Thermal stresses in the coating due to temperature changes were obtained. The effects of micro channel geometry on thermal stresses were studied in detail. The results revealed that in order to increase the mechanical performance of the coatings, film thickness and profile geometry must be optimized. Future work should illustrate the optimization analysis in detail. For example, the relationship between the round corner radius and the stress distribution can be obtained. Besides, the effect of z direction along the micro channel length should be taken into account to make the simulation closer to the conditions in practice.

References

1. A.C. Fischer-Cripps, *Nanoindentation*. 2004, New York: Springer.
2. Encyclopedia Britannica Online.
<http://www.britannica.com/EBchecked/topic/387714/Mohs-hardness>, 2009.
3. A.A. Volinsky, D.F. Bahr, M.D. Kriese, N.R. Moody, and W.W. Gerberich, *Nanoindentation Methods in Interfacial Fracture Testing*, Chapter 13 in *Comprehensive Structural Integrity* (I. Milne, R.O. Ritchie, B. Karihaloo, Editors-in-Chief), Volume 8: *Interfacial and Nanoscale Failure*. 2003: Elsevier.
4. W.C. Oliver and G.M. Pharr, An improved technique for determining hardness and elastic modulus using load and displacement sensing indentation experiments. *J. Mater. Res.*, 1992. 7(6): p. 1564.
5. W.C. Oliver and G.M. Pharr, Measurement of hardness and elastic modulus by instrumented indentation: Advances in understanding and refinements to methodology. *J. Mater. Res.*, 2004. 19: p. 3.
6. M. Qasmi, P. Delobelle, F. Richard, C. Brun, and M. Fromm, Viscoelastic mechanical properties determined by nanoindentation tests and its numerical modelling of polypropylene modified by He⁺ particle implantation and e-irradiation. *Progress in Organic Coatings*, 2004. 51(3): p. 195.
7. K.L. Johnson, *Contact Mechanics*. 1985: Cambridge University Press.
8. H. Hertz, On the contact of elastic solids. *J. Reine Angew. Math.*, 1881. 92: p. 156-171.
9. H. Hertz, On hardness. *Hertz's Miscellaneous Papers*. 1896, London: Macmillan & Co.
10. P. Waters, *Stress analysis and mechanical characterization of thin films for microelectronics and MEMS applications* (PhD Thesis). 2008, University of South Florida.
11. A.C. Fischer-Cripps, *Introduction to Contact Mechanics*. 2000, New York: Springer.

12. E.S. Berkovich, Three-faceted diamond pyramid for micro-hardness testing. *Ind. Diamond Rev.*, 1951. 11(127): p. 129-133.
13. M. Lichinchi, C. Lenardi, J. Haupt, and R. Vitali, Simulation of Berkovich nanoindentation experiments on thin films using finite element method. *Thin Solid Films*, 1998. 312(1-2): p. 240.
14. C. Walter, T. Antretter, R. Daniel, and C. Mitterer, Finite element simulation of the effect of surface roughness on nanoindentation of thin films with spherical indenters. *Surface and Coatings Technology*, 2007. 202(4-7): p. 1103.
15. J. Chen and S.J. Bull, On the relationship between plastic zone radius and maximum depth during nanoindentation. *Surface and Coatings Technology*, 2006. 201(7): p. 4289.
16. C. W. Shih, M. Yang, and J.C.M. Li, Effect of tip radius on nanoindentation. *J. Mater. Res.*, 1991(6): p. 2623.
17. E. Donnelly, S.P. Baker, A.L. Boskey, and M.C.H.v.d. Meulen, Effects of surface roughness and maximum load on the mechanical properties of cancellous bone measured by nanoindentation. *J. Biomed. Mater. Res. A.*, 2006 May. 77(2): p. 426-435.
18. A. Bolshakov and G.M. Pharr, Influences of pileup on the measurement of mechanical properties by load and depth sensing indentation techniques. *J. Mater. Res.*, 1998. 13(4): p. 1049-1058.
19. X. Huang and A.A. Pelegri, Finite element analysis on nanoindentation with friction contact at the film/substrate interface. *Composites Science and Technology*, 2007. 67(7-8): p. 1311-1319.
20. M. Bai, K. Kato, N. Umehara, and Y. Miyake, Nanoindentation and FEM study of the effect of internal stress on micro/nano mechanical property of thin CNx films. *Thin Solid Films*, 2000. 377-378: p. 138.
21. K.H. K, N.M. Jennett, W. Wegener, J. Meneve, K. Hasche, and R. Seemann, Progress in determination of the area function of indenters used for nanoindentation. *Thin Solid Films*, 2000. 377: p. 394-400.
22. N. Yu, A.A. Polycarpou, and T.F. Conry, Tip-radius effect in finite element modeling of sub-50 nm shallow nanoindentation. *Thin Solid Films*, 2004. 450(2): p. 295.
23. Ford, *Advanced Mechanics of Materials*. 1963, London: Longmans.
24. A.C. Ugural and S.K. Fenster, *Advanced Strength and Applied Elasticity*. Third ed. 1995: Prentice-Hall PTR.
25. S. Timoshenko, *Theory of Elasticity*. 1970: McGraw-Hill Companies.

26. O.C. Zienkiewicz and R.L. Taylor, *The Finite Element Method* Set. 2005: Butterworth-Heinemann.
27. J.D. Bressan, A. Tramontin, and C. Rosa, Modeling of nanoindentation of bulk and thin film by finite element method. *Wear*, 2005. 258(1-4): p. 115.
28. A.A. Pelegri and X. Huang, Nanoindentation on soft film/hard substrate and hard film/soft substrate material systems with finite element analysis. *Composites Science and Technology*, 2008. 68(1): p. 147-155.
29. X. Li, B. Bhushan, K. Takashima, C.-W. Baek, and Y.-K. Kim, Mechanical characterization of micro/nanoscale structures for MEMS/NEMS applications using nanoindentation techniques. *Ultramicroscopy*, 2003. 97(1-4): p. 481.
30. M.C. Fivel, C.F. Robertson, G.R. Canova, and L. Boulanger, Three-dimensional modeling of indent-induced plastic zone at a mesoscale. *Acta Materialia*, 1998. 46(17): p. 6183.
31. H. Pelletier, J. Krier, and P. Mille, Characterization of mechanical properties of thin films using nanoindentation test. *Mechanics of Materials*, 2006. 38(12): p. 1182.
32. J.A.Knapp, D.M.Follstaedt, S.M.Myers, J.C.barbour, and T.A.Friedmann, Finite element modeling of nanoindentation. *Journal of Applied Physics*, 1999. 85(3).
33. J.A. Knapp, D.M. Follstaedt, S.M. Myers, J.C. Barbour, T.A. Friedmann, J.W. Ager, O.R. Monteiro, and I.G. Brown, Finite-element modeling of nanoindentation for evaluating mechanical properties of MEMS materials. *Surface and Coatings Technology*, 1998. 103-104: p. 268.
34. D. Ma, K. Xu, and J. He, Numerical simulation for determining the mechanical properties of thin metal films using depth-sensing indentation technique. *Thin Solid Films*, 1998. 323(1-2): p. 183.
35. Y. Sun, T. Bell, and S. Zheng, Finite element analysis of the critical ratio of coating thickness to indentation depth for coating property measurements by nanoindentation. *Thin Solid Films*, 1995. 258(1-2): p. 198.
36. K.C. Tang, A. Faulkner, N. Schwarzer, R.D. Arnell, and F. Richter, Comparison between an elastic-perfectly plastic finite element model and a purely elastic analytical model for a spherical indenter on a layered substrate. *Thin Solid Films*, 1997. 300(1-2): p. 177.
37. J.L. He and S. Veprek, Finite element modeling of indentation into superhard coatings. *Surface and Coatings Technology*, 2003. 163-164: p. 374-379.
38. W.D.Callister, *Materials Science and Engineering*. 2000, New York: Wiley.
39. ANSYS 11.0 user manual. ANSYS Inc. 2007.

40. K. Du, X. Pang, C. Chen, and A.A. Volinsky, Mechanical Properties of Evaporated Gold Films. Hard Substrate Effect Correction. Mat. Res. Soc. Symp. Proc. , 2008. 1086E, U8.41.
41. A.A. Volinsky, N.R. Moody, and W.W. Gerberich, Interfacial Toughness Measurements for Thin Films on Substrates. Acta Materialia, 2002. 50(3): p. 441-466.
42. A.A. Baker, L.R.F. Rose, and R. Jones, Advances in the Bonded Composite Repair of Metallic Aircraft Structure. 2002: Elsevier Science.
43. J.L. Beuth, Cracking of thin bonded films in residual tension. International Journal of Solids and Structures, 1992. 29(13): p. 1657.
44. J.L. Beuth, Fracture analyses of thin films, interfaces and joints (Ph.D thesis). 1992, Harvard University.
45. S. Mall and S. Naboulsi, Modeling of a cracked metallic structure with bonded composite patch using the three layer technique. Composite Structures, 1996. 35 (3): p. 295-308.
46. S. Naboulsi and S. Mall, Nonlinear analysis of bonded composite patch repair of cracked aluminum panels. Composite Structures, 1998. 41 (3-4): p. 303-313.
47. D.-C. Seo and J.-J. Lee, Fatigue crack growth behavior of cracked aluminum plate repaired with composite patch. Composite Structures, 2002. 57 (1-4): p. 323-330.
48. W.-Y. Lee and J.-J. Lee, Successive 3D FE analysis technique for characterization of fatigue crack growth behavior in composite-repaired aluminum plate Composite Structures 2004. 66(1-4): p. 513-520.
49. S.K. Chan, I.S. Tuba, and W.K. and Wilson, On the finite element method in linear fracture mechanics. Engineering Fracture Mechanics, 1970(2): p. 1-17.
50. Kobayashi, A.S., D. Maiden, B. Simon, and S. Iida, Application of finite element analysis method to two-dimensional problems in fracture mechanics. ASME Winter Annual Meeting, Nov.1969.
51. C.T. Sun, J. Klug, and C. Arendt, Analysis of cracked aluminum plates repaired with bonded composite patches. AIAA Journal, 1996. 34(2): p. 369-374.
52. W.-T. Chau, Bonded repair of a center-cracked panel with composite patches (PhD Thesis). 2000, Hong Kong University of Science and Technology.
53. J.J. Schubbe and S. Mall, Modeling of cracked thick metallic structure with bonded composite patch repair using three-layer technique Composite Structures, 1999. 45(3): p. 185-193.
54. Y. Murakami, Stress Intensity Factors Handbook. 2003: Elsevier Science Ltd.

55. F. Endogan and M.M. Ratwani, Stress distribution in bonded joints. *Journal of Composite Materials*, 1971. 5: p. 378-393.
56. P. Papanikos, K.I. Tserpes, G. Labeas, and S. Pantelakis, Progressive damage modelling of bonded composite repairs. *Theoretical and Applied Fracture Mechanics*, 2005. 43(2): p. 189-198.
57. P. Colombi, A. Bassetti, and A. Nussbaumer, Delamination effects on cracked steel members reinforced by prestressed composite patch. *Theoretical and Applied Fracture Mechanics*, 2003. 39(1): p. 61-71.
58. P. Watts and C. Wiles, Recent advances in synthetic micro reaction technology. *Chemical Communications*, 2007: p. 443-467.
59. World Wide Web. [Http://www.aalco.co.uk/technical/stainless.html](http://www.aalco.co.uk/technical/stainless.html).
60. World Wide Web.
[Http://www.matthey.ch/fileadmin/user_upload/downloads/fichetechnique/EN/1.4_301.pdf](http://www.matthey.ch/fileadmin/user_upload/downloads/fichetechnique/EN/1.4_301.pdf).
61. World Wide Web.
[Http://www.aalco.co.uk/technical/datasheets/Aalco_Datasheet_St_St_304.pdf](http://www.aalco.co.uk/technical/datasheets/Aalco_Datasheet_St_St_304.pdf).
62. World Wide Web. <http://www.accuratus.com/fused.html>.
63. World Wide Web.
<http://www.virginiasemi.com/pdf/generalpropertiesSi62002.pdf>.
64. M. Ogura, H. Miyoshi, S.P. Naik, and T. Okubo, Investigation on the Drying Induced Phase Transformation of Mesoporous Silica; A Comprehensive Understanding toward Mesophase Determination. *Journal of the American Chemical Society*, 2004. 126(35): p. 10937–10944.
65. M.-C. Liu, H.-S. Sheu, and S. Cheng, Drying induced phase transformation of mesoporous silica. *Chemical Communications*, 2002: p. 2854–2855.
66. Y. Zhong and T. Zhu, Simulating nanoindentation and predicting dislocation nucleation using interatomic potential finite element method. *Computer Methods in Applied Mechanics and Engineering*, 2008. 197(41-42): p. 3174-3181.
67. T. Zhu, J. Li, K. J. Van Vliet, S. Ogata, S. Yip, and S. Suresh, Predictive modeling of nanoindentation-induced homogeneous dislocation nucleation in copper. *Journal of the Mechanics and Physics of Solids*, 2004. 52(3): p. 691-724.
68. K.D. Bouzakis, N. Michailidis, and G. Skordaris, Hardness determination by means of a FEM-supported simulation of nanoindentation and applications in thin hard coatings. *Surface and Coatings Technology*, 2005. 200(1-4): p. 867-871.
69. J. Hutchinson and Z. Suo, Mixed-mode cracking in layered materials. *Advances in Applied Mechanics*, 1992. 29: p. 63-191.

70. K.M. Liechti and Y.S. Chai, Asymmetric shielding in interfacial fracture under in-plane shear. *Journal of Applied Mechanics*, 1992. 59: p. 295-304.